Comparison of focused and Fourier transform ultrasound optical tomography

by Angad Singh

LUND
UNIVERSITY

Thesis for the degree of Master's in Physics
LRAP624(2026)
Project duration: September 2025 - May 2026
Division of Atomic Physics
Thesis advisors: Nina Reistad, Stefan Kröll and Alexander Bengtsson

Contents

Acknowledgements

First and foremost, I would like to thank my supervisors, Nina Reistad, Stefan Kröll, and Alexander Bengtsson, without whom this project would not have been possible. Nina taught me how to stay organized, communicate my science clearly and through her I also learnt the art of phantom making. Stefan's door was always open (literally, as I sat in the office across from him) for discussions, insightful questions and thoughtful answers. I am very grateful to Alexander for "taking me under his wing" and patiently answering a lot of my silly (maybe sometimes good) questions whenever I had them. I have learnt a lot about UOT, spectral hole burning and how to be a great researcher through him.

I would also like to thank the members of the Quantum Information group at the division of Atomic Physics, and especially my office-mates Johannes, Erik, Mira, Felix, Jakob and Yash for their company during "work" and fika. Equal thanks go to the researchers at Deep Light Vision, Cornelia, David and Maria, who genereously and patiently shared their company, knowledge of UOT and research as a whole. I would also like to thank Stefan Šušnjar for very fruitful discussions regarding the simulations.

A special thanks to François Ramaz, Jean-Michel Tualle and Rishabh Sharma at the Langevin Institute in Paris for hosting me, guiding my experiments, and teaching me so much about Fourier transform UOT and experimental work.

My friends here in Lund have been a constant source of support and encouragement. Thank you for putting up with my bad jokes all the time and making Sweden feel like a home away from home. My friends back in India were also a wonderful source of comfort and dependence during tough times.

Finally, to my family - Maa, Paa and Simran di- thank you from the bottom of my heart. This entire journey would not have been possible without you and your constant support.

Abstract

Ultrasound optical tomography (UOT) combines the high contrast of optical imaging with the spatial resolution of ultrasound, making it a promising modality for imaging in scattering media. Conventionally, UOT relies on focused ultrasound to localize the acousto-optic interaction. An alternative approach, Fourier-transform UOT (FT-UOT), has been proposed to encode spatial information using spatially structured ultrasound fields, which enables imaging over larger volumes simultaneously.

The aim of this thesis is to investigate the feasibility of FT-UOT as an alternative to the focused ultrasound regime. Both a simulation framework and an experimental implementation are developed and tested. The simulation is based on a diffusion approach and is used to evaluate the theoretical performance of FT-UOT in reconstructing spatial features of absorbing inclusions. Experimentally, FT-UOT is implemented using a photorefractive detection scheme and compared directly with the focused ultrasound approach using tissue-mimicking phantoms.

The simulation results demonstrate that FT-UOT is, in principle, capable of recovering spatial information comparable to that obtained with focused ultrasound. However, experimental results show that the image quality in FT-UOT is currently limited by factors like inaccuracies in the generated acoustic field and longer acquisition times. Improvements in signal detection led to a significant enhancement in image quality and which enabled the visualization of inclusion features using FT-UOT.

Overall, this work shows that while FT-UOT is a feasible imaging approach with a strong theoretical foundation, but using the current experimental implementation does not yet outperform the focused ultrasound regime. The results identify challenges related to ultrasound field generation, reconstruction, hardware optimization, and highlight important directions for future development.

Popular science summary

Many medical imaging techniques that use light suffer from a fundamental challenge of not being able to "see" deep inside the body. Light is highly scattering inside the body, limiting how deep we can "see" to around 2 cm. An easy way to understand this is by holding up a flashlight to your fingertips. Light clearly passes through, leaving behind a warm red hue, yet you cannot see any visual indication of the bone in your finger.

To overcome this imaging problem, many other techniques or "modalities" of imaging have been invented that exploit other properties of the body to create an image. A few examples of this are ultrasound, magnetic resonance imaging (MRI), positron emission tomography (PET), and computed tomography (CT). However, these techniques themselves have drawbacks of being expensive, unsuitable for repeated use, or providing limited contrast for certain tissue types.

To tackle this challenge, a new technique called ultrasound optical tomography (UOT) was developed to combine the best of both worlds, the rich contrast that light provides and the penetration depth ultrasound can reach. In UOT, pulses of light and ultrasound are sent into the body simultaneously. The ultrasound shifts the "colour" or frequency of the light by a tiny amount in the region where the two overlap, effectively "tagging" the light and marking exactly where it has been. Using a special material called photorefractive crystal, the tagged light is filtered out and used to reconstruct an image from deep inside the body. Currently, UOT builds images one point at a time by focusing the ultrasound to a single spot and tracking its propagation. This is slow and produces only a small amount of tagged light.

This work explores a new approach, that instead of using a focused ultrasound pulse, the ultrasound is sent into the tissue in a structured pattern that is able to cover a much larger area at once. The image is then reconstructed with the help of a mathematical tool called the Fourier transform. Fourier transforms are used everywhere in our lives and even in other medical imaging techniques like MRI and CT scan. A simple way to understand what the Fourier transform does is the following: imagine you have a model made out of LEGO bricks that you want to recreate. You could examine the model one brick at a time, which would take a lot of time. Or you could ask a better question, how many 3×3 blue pieces exist in the model, or how many 3×4 green ones there are? The Fourier transform works similarly, it helps you extract global patterns. In terms of UOT, this means more tagged light and possibly faster image formation. Ultimately, the goal of this work is to bring UOT closer to real clinical use, particularly for the detection and diagnosis of breast cancer, and hopefully in the future, monitoring of oxygen level in the heart.

List of abbreviations

US	-	Ultrasound
PAI	-	Photoacoustic imaging
UOT	-	Ultrasound optical tomography
FT-UOT	-	Fourier transform ultrasound optical tomography
UV	-	Ultraviolet
NIR	-	Near-infrared
AOT	-	Acousto-optic tomography
PR	-	Photorefractive
SNR	-	Signal-to-noise ratio
AgI	-	Agar-intralipid
SEBS	-	Styrene-ethylene / butylene-styrene
PTOFS	-	Photon time-of-flight spectroscopy
FT-AOT	-	Fourier transform acousto-optic tomography
MOPA	-	Master oscillator power amplifier
SPS:Te	-	$Sn_2P_2S_6$ doped with 1% Te
APD	-	Avalanche photodiode

Chapter 1

Introduction

Medical imaging aims to uncover the structural details of the human body using a range of physical principles. It has become an indispensable tool in the early detection, diagnosis and treatment of diseases. Its development has been occurring for about 130 years, beginning in 1895 with Wilhelm Röntgen's discovery of x-rays [1], which enables non-invasive visualization of bone structures deep within the body [2–4]. Since then, scientific curiosity and clinical needs have driven the development of advanced imaging modalities.

Among these, computed tomography, developed in the 1970's, helps in the reconstruction of a two-dimensional image of a part of the body with the aid of a rotating x-ray source and detector system [5, 6]. Magnetic resonance imaging relies on strong magnetic fields and radio frequency pulses to polarize and excite protons in the body, with differences in relaxation times providing soft tissue contrast [3, 7]. Ultrasound (US) imaging exploits differences in acoustic impedances between different tissue interfaces to generate real time images [8]. While each of these techniques has significantly advanced medical diagnostics, they also present various inherent limitations like, high costs, long imaging and acquisition times, limited contrast in certain cases, or potential risks with repeated exposure.

Optical imaging is an attractive modality for medical imaging and diagnosis as it provides contrast that arises from the complex interaction between light and biological matter. It also offers an additional advantage of being non-harmful (within safe exposure limits). However, the highly scattering nature of visible and near infrared light within biological matter reduces its penetration depth significantly. As a result, optical imaging techniques were restricted to superficial structures, such as the skin or the retina. Beyond depths of approximately 1 mm, light loses its original directionality

and as a consequence, its spatial resolution. Techniques such as diffuse optical tomography [9, 10] and optical coherence tomography [11, 12], while valuable, are therefore limited by poor spatial resolution or restricted imaging depth [13].

These limitations necessitate the need for non-invasive optical imaging techniques that are capable of probing deeper into biological tissue while preserving optical contrast. Developments in US-aided optical imaging techniques, like photo-acoustic imaging (PAI) [14, 15] or ultrasound optical tomography (UOT) [13, 16, 17], have emerged as promising solutions. PAI relies on short bursts of laser pules to irradiate target tissue, where the absorption of light pulses causes thermomechanical expansion releasing an acoustic wave, which is detected externally. In contrast, UOT is a medical imaging technique that uses a combination of light and sound to increase the depth of the imaging to several centimeters. This technique combines the advantages of optical properties, namely, contrast—with those of US, which provides spatial resolution [13]. In UOT, the tissue is irradiated with optical laser light along with pulses of US. The interaction between these two fields causes the light to shift in frequency, "tagging the photons", via an acousto-optical effect. By detecting this tagged light, information about the optical properties of the region defined by the US field can be studied. UOT has potential applications in areas like breast cancer imaging and detection, monitoring heart oxygenation, brain imaging, and more [16, 18].

Conventionally, UOT is performed using a focused US pulse that is scanned sequentially through the tissue, building an image line-by-line. Fourier transform ultrasound optical tomography (FT-UOT) offers an alternative approach by using spatially structured US fields, which simultaneously tag photons across a larger volume. An image is then reconstructed with the ensemble of measurements through an inverse Fourier transform, potentially leading to increased signal while preserving the advantage of optical contrast of UOT.

1.1 Aim and outline of thesis

The aim of this work is to investigate the feasibility of FT-UOT as an alternative approach to the conventional focused US approach, with respect to image quality, signal strength and practical implementation. To do this, a diffusion-based simulation is used to study the theoretical performance of FT-UOT. FT-UOT is also implemented experimentally using a photorefractive detection scheme, and the results are directly compared with the conventional approach. The limitations,strengths and practical challenges of FT-UOT are then identified and discussed.

This thesis is organized as follows. Chapter 2 introduces fundamental concepts re-

lated to light-tissue interactions, sound propagation in tissue and physical mechanisms used to understand UOT. Chapter 3 describes the detection scheme, fabrication of phantoms and experimental setup. It also provides an overview of the two imaging approaches used in this work. Chapter 4 presents the simulation framework used to model FT-UOT, and these results are used to discuss the theoretical feasibility of the method. Chapter 5 presents the experimental results obtained using both the focused US regime and FT-UOT. Chapter 6 summarizes the main findings, discusses the limitations and provides possible directions of future research.

Chapter 2

Light, sound and their interaction in tissue

UOT deals with the propagation of light, sound and their interaction within biological tissue. An overview of each of the mechanisms is therefore necessary to understand how it can be used for non-invasive optical diagnostic imaging. This chapter introduces the principles of light and sound propagation in tissue, and the acousto-optic interactions that help form the basis of UOT.

2.1 Light propagation in tissue

The two primary interactions that are relevant within tissue are absorption and scattering of light. Reflection and refraction are more relevant at surfaces which occur due to differences in material bulk properties. Figure 2.1 shows the basic interactions between light and tissue.

2.1.1 Absorption

Absorption determines how strongly light is attenuated while it travels through tissue. This property is highly dependent on the wavelength of light and the molecular composition of the tissue [19]. Consequently, choosing an appropriate wavelength is essential and must be tailored to the type of application in mind. At a fundamental level, absorption is dictated by the difference in the energy levels of the molecules involved in the interaction. When a particular wavelength of light is absorbing, the

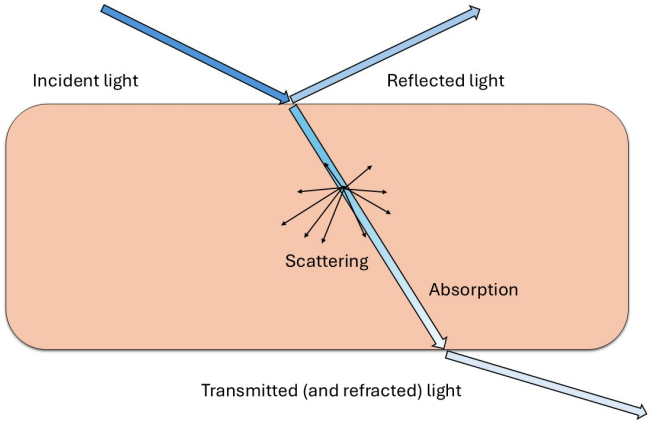

Figure 2.1: Basic light-tissue interactions.

energy is converted into heat. This is then used for different thermal interactions, such as ablation and coagulation.

To quantify light absorption, the coefficient of absorption (μ_a) is used. It defines the probability of a photon being absorbed per unit path length for a specific material [19, 20]. The absorption coefficient has units of $[L]^{-1}$, commonly expressed as cm^{-1} or mm^{-1} in biological tissue. Its inverse is called the absorption mean free path or absorption length, $l_a = 1/\mu_a$, and expresses the average distance a photon covers before being absorbed. The intensity of light when passing through tissue attenuates exponentially, and follows Beer-Lambert's Law,

$$I(x) = I_0 \mathrm{e}^{-\mu_a x}, \tag{2.1}$$

where I is the intensity of light, x is the distance within the tissue, I_0 is the initial intensity of the incident light on the material, and μ_a is the absorption coefficient.

In tissue, absorption occurs due to many different constituents, but the major contributors are water and macromolecules such as proteins [19]. Water is the main absorber in the infrared region, which is important because it constitutes a major fraction in most tissues. In the visible and UV regions, macromolecules such as proteins, melanin and hemoglobin are the predominant absorbers [19]. Oxygenated hemoglobin or oxyhemoglobin (HbO_2) and deoxyhemoglobin (Hb) have different absorption spectra (see figure 2.2). This happens because there are structural changes in hemoglobin when it binds to oxygen. Figure 2.2 shows the absorption coefficients of tissues components. Below 600 nm, both oxyhemoglobin and deoxyghemoglobin have strong absorption of light, making wavelengths below 600 nm practically impractical for imaging deeper parts of the body. Similarly, the high absorption of light by water of wavelengths greater than 950 nm causes these wavelengths to be ineffective for deep

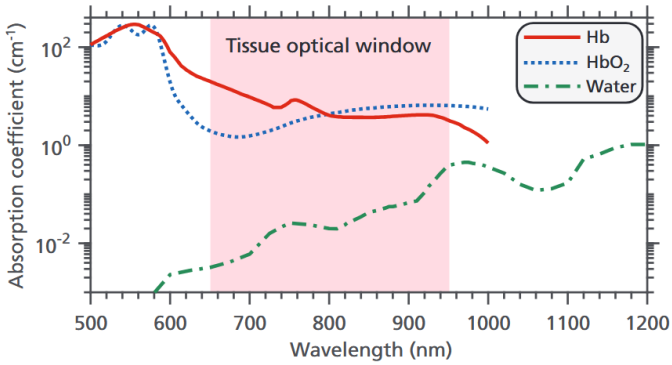

Figure 2.2: Absorption coefficient of deoxygenated blood (Hb), oxygenated blood (HbO_2) and water as a function of wavelengths. The tissue optical window is highlighted, showing the reduced absorption in this region making optical imaging possible. Image taken from [21].

tissue imaging.

This opens up a small window of wavelengths, known as the tissue optical window or therapeutic window, between $650 - 950$ nm which allows for the most optimal penetration of light. Other windows have also been identified and discussed in literature [22, 23] due to tissue autofluorescence in the first optical window [23] and lower scattering in tissue at longer NIR wavelengths [22]. In the present work, we focus on the window from $650 - 950$ nm, the first optical tissue window.

2.1.2 Scattering

Light scatters the most when it encounters structures with refractive indices different from its surroundings, causing it to deviate from its initial straight trajectory. Scattering of light is the most dominant when its wavelength is comparable to the size of the object off which it scatters [19, 24]. The phenomenon of scattering in biological media is complex due to the presence of intricate structures and inhomogeneities. This causes the light to lose spatial information due to the randomization of paths as it travels through the tissue, giving rise to the problem of not being able to use light for imaging tissue in deep parts of the body; a problem UOT is trying to overcome.

The scattering process can be elastic or inelastic. Elastic scattering conserves energy between the incident photon and scattered photon, whereas inelastic scattering does not. When photons scatter inelastically, there is an energy exchange between the photon and the interacting molecule. This energy can be transferred from the photon to the molecule or vice-versa. This is used in many different bio-analysis techniques like stimulated Raman scattering, coherent anti-stokes Raman scattering, and fluorescence based spectroscopy [19, 20]. However, the majority of the light-tissue interactions are

elastically scattering [19], and therefore this will be the focus of further discussion. Scattering in tissue stems from the interaction between a whole range of biological structures and light; from the entirety of the cell, down to the cell membrane. Cell nuclei and mitochondria are the main scatters in cells [19, 24].

Similarly to absorption, scattering is quantified with the scattering coefficient μ_s. It defines the probability of a photon being scattered per unit path length for a specific material. It is also commonly measured in units of cm^{-1} or mm^{-1} in the context of biological tissue. Its inverse, l_s, is the scattering mean free path, defines the average distance a photon travels between two scattering events.

Scattering in tissue is explained by Mie and Rayleigh scattering, as there are scatters of different sizes that are responsible for the phenomenon. Rayleigh scattering is only valid when the size of the particles is smaller than the wavelength of light, small enough so that the electric field can be assumed to be homogeneous inside the particle [20]. This translates to $a << \lambda/2\pi$, a being the size of the particle and λ the wavelength of light. Mie scattering deals with scattering by basic shapes like spheres using the Maxwell's equations. It is valid for isotropic homogeneous spheres of any size and refractive index, when irradiated with light of any wavelength [19, 20, 24]. This theory reduces down to Rayleigh scattering when the small particle size condition is satisfied. Although the scatters in tissues are not perfect spheres, their behaviour can be explained quite well using the Mie theory of scattering.

The Mie theory of scattering shows that the scattering in tissue is highly anisotropic, and is primarily forward scattering. This anisotropy is expressed by the anisotropy factor, which is defined as

$$g = \langle \cos\theta \rangle \,, \tag{2.2}$$

where θ is the scattering angle[1]. For $g = 0$, we have isotropic scattering, $g = 1$ for total forward scattering, and $g = -1$ for total back scattering. The g values for biological tissue are in the range $0.7 - 0.9$ [25]. This is used to define the reduced scattering coefficient

$$\mu_s' = \mu_s(1 - g). \tag{2.3}$$

This couples the scattering to its direction and is useful in the diffusive regime [2] (more about it in chapter 4), which is relevant in tissues due to them being heavily scattering in nature. It is common to define $l_s' = 1/\mu_s'$ which represents the distance travelled by a photon before losing its original directionality. Figure 2.3 explains the difference between l_s and l_s'.

[1] The angle the light has deviated after a scattering.

[2] $\mu_a << \mu_s'$

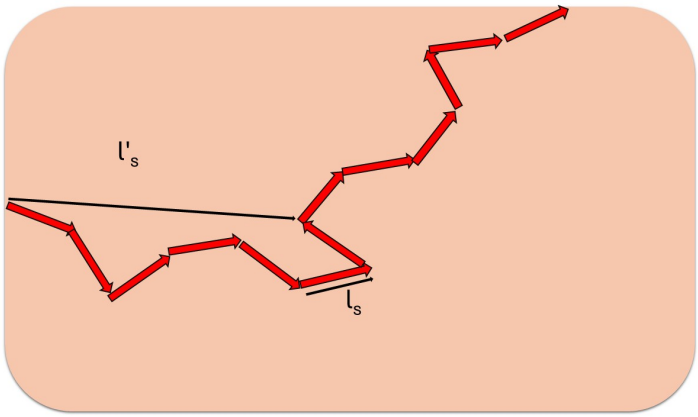

Figure 2.3: Difference between scattering coefficient (μ_s) and reduced scattering coefficient (μ_s'), shown via their inverses, scattering mean free path (l_s) and transport mean free path (l_s').

2.1.3 Speckles

A diffusive medium, like biological tissue, when illuminated with a coherent light source, will form a random pattern of varying intensity (dark and bright spots), called a speckle. This happens because of random interference caused by the scatters in the diffusive media. This is usually considered to be a negative feature due to its random and noise-like feature; and a hindrance in techniques like radar, optical coherence tomography and US. However, it has been used successfully in different techniques such as laser speckle contrast imaging, to help build blood flow maps [26–28] and electronic speckle pattern interferometry [29]. In tissue, this speckle pattern is dynamic due to the fact that scattering particles themselves are moving, through motion caused by like blood flow or breathing. This is called speckle decorrelation. In human tissue, this occurs on the time scale $\sim 0.1 - 1$ ms [31, 32]. This decorrelation puts a time limit on how fast the UOT signal must be captured for *in-vivo* measurements for techniques that are sensitive to speckle decorrelation. This will be discussed further in the discussion about the UOT setup with the photo-refractive crystal detection in chapter 3. An example of a speckle pattern is shown in figure 2.4.

2.2 Sound propagation in tissue

US is a high frequency sound wave that has been used not only for diagnostic imaging but also for therapeutic purposes. For diagnostic purposes, the frequency range commonly utilized is $2 - 15$ MHz [8]. In classical US imaging, the image is created through echoes that are formed by the reflection of acoustic waves when it experiences

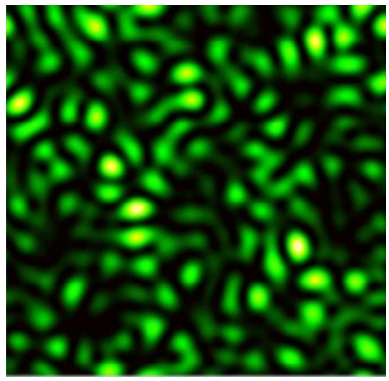

Figure 2.4: Formation of a speckle pattern after coherent light passes through a diffusive medium [30]

tissues boundaries with different acoustic impedances. Acoustic impedance describes the resistance of a material to transmission of sound. It is given by $z = p/v$ where p is the local pressure and v is the local particle velocity. The difference in acoustic impedance for different tissue types determines how much energy of the acoustic wave gets reflected versus passes an interface between two types of tissue. This provides the US contrast between two tissue of types in an US image.

The speed of sound in a material is dependent on two factors; its stiffness (how easily it is deformed) and its density. In tissue, the speed of an acoustic wave is 1540m/s [3], and this is the value used for most simulations and calculations. Acoustic waves behave very similarly to light waves. They follow a few of the same rules which govern the light waves, such as law of reflection, Snell's law[4], and even Raleigh scattering [8][5], when the condition of Rayleigh scattering is met.

The attenuation of sound waves is dependent on the absorption (which is converted to heat), scattering, reflection and divergence of the beam as it propagates. The dependence of the attenuation of acoustic waves in tissue increases with frequency [8], and is almost linear when expressed in dB cm^{-1}. This is a fact to keep in mind as higher frequencies are able to provide better resolution but not a great penetration depth. Therefore, a compromise[6] needs to be reached with the required resolution and penetration depth.

[3] This is an average, as different tissues will have different densities and stiffnesses.

[4] When the acoustic wave experiences a medium with a different acoustic impedance.

[5] Scattering strength $\propto \lambda^{-4}$.

[6] The reflected sound wave produced at a boundary or scatterer will also be attenuated as it is reaching back to the US transducer.

2.3 Light and sound interaction

The acoustic-optic effect deals with the interaction between coherent light and sound. This effect has been known for around 90 years, as it was initially theorized by Brillouin in 1922 [33] and experimentally proven by Debye and Sears [34], along with Lucas and Biquard ten years later [35]. This effect is explained by the change in refractive index caused by the passing of the acoustic wave through the medium. This can lead to deflection, intensity and phase modulation and, most important for this thesis, frequency shifting of the light. Along with present-day applications in, acousto-optic modulators, deflectors and signal processing, it has applications in the field of biomedical imaging through a new form of non-invasive imaging modality, called **ultrasound optical tomography**.

2.4 Ultrasound Optical Tomography

UOT, sometimes also referred to as acousto-optical tomography (AOT), is based on modulation of light through US. The issue with other optical imaging techniques, is that biological tissue is highly scattering in nature, which not only limits the possible imaging depth, but also makes you lose spatial information about where the light has been in the tissue; losing the optical contrast light can provide in tissue. To combat this problem, UOT uses US to "tag" the light. This tagging is, usually[7], focused on a certain volume in the tissue, providing information about where the light is coming from in the tissue.

The tissue is irradiated with laser light, of frequency f_{L}, along with US pulses, of frequency f_{US}. The interaction between these two fields causes the light to shift in frequency, "tagging the photons", via the acousto-optical effect [13, 16, 17]. The tagged, or modulated, photons will be frequency shifted by $\pm f_{\mathrm{US}}$, or by higher harmonics of the acoustic frequency.

Detection of these tagged photons is the biggest challenge in UOT. As the frequency of the US is very small (in the order of MHz) compared to the frequency of the carrier light (in the order of 100 THz), the relative shift in the carrier frequency (laser light) is very small. Practically, this corresponds to detecting a shift of $\sim 10^{-5}$nm at a wavelength of $\sim$ 700nm. No traditional optical filters are able to achieve this level of precision, which necessitates the use of interferometric and other high resolution spectral separation techniques [16].

The other major challenge in the detection of the modulated signal (tagged light) from

[7] More about this in chapter 3.

the background signal of unmodulated light is caused by the fact, that the amount of light which is tagged is also very small. The fraction of photons that get tagged is around $10^{-3} - 10^{-5}$ [21]. Tagged photons also scatter and exit the tissue from various different directions; the emission *etendue* [8] is substantial. To recover the maximum amount of tagged photons, to maximize the UOT signal, the *etendue* of the detection scheme and system should be large.

Multiple detection schemes have been developed to filter tagged light photons from the sea of untagged photons. They can be broadly classified into two main categories: coherent and incoherent. Coherent detection methods are susceptible to speckle decorrelation[9], which can be a problem for *in vivo* applications as these methods are dependent on the temporal coherence of speckles [36]. Some examples of coherent detection methods are digital holography, parallel speckle processing, and photorefractive crystals [16, 37]. Incoherent techniques include Fabry-Perot interferometry [38] and spectral hole burning filters [39–41]. These detection methods are extensively discussed and compared in literature [16, 17, 21, 36, 37, 42], but in the context of this thesis, the focus will be on using photorefractive crystals for the detection of modulated light.

2.4.1 Mechanism

The theory of UOT was developed by Wang [43, 44], explaining the three mechanisms responsible for the modulation of light via US pulses.

1. Change in optical properties - the pressure changes caused by the US as it propagates through the medium causes the optical properties, scattering and absorption coefficients, to change. This is possible without the coherence of light. The signal produced by this mechanism is very weak, and usually ignored when making analytical models and simulations [42, 44, 45].

2. Change in optical phase due to displacement of scatters - the movement of scatters due to the US changes the optical path length, modulated at the frequency of the US, leading to an optical phase modulation.

3. Change in optical phase due to modification of refractive index - the pressure wave creates fluctuations in density, resulting in a periodic change in refractive index. This leads to a change in the optical path length, modulating the optical

[8] Given by the product between the area of the emitting surface and solid angle extended by the emitted light

[9] See section 2.1.3

phase. The refractive index is assumed to vary linearly [45, 46]with pressure as

$$n(t, \mathbf{r}) = n_0(1 + \frac{\partial n}{\partial P} P(t, \mathbf{r})), \tag{2.4}$$

where n is the refractive index, P the time-dependent pressure field, and $\frac{\partial n}{\partial P}$ the piezo-optic coefficient.

The second and third mechanisms require the use of coherent light. The third mechanism begins to dominate the second mechanism at higher US frequencies ($1 - 5$ MHz) [43, 45, 46], which are considered ideal for UOT [16].

2.4.2 Principle of UOT

UOT spatially encodes or tags light using US, as it shifts the frequency from f_{L} to $f_{\mathrm{L}} \pm n f_{\mathrm{US}}$ ($n \in \mathbb{N}$), which is later detected using one of the many possible techniques. The amount of tagged photons depends on the optical properties, like absorption and scattering, acoustic properties, and the optical fluence in the US volume [36]. Therefore, the information provided by the tagged photons belongs to insonified volume of tissue. Moving the insonified volume to different locations makes it possible to form an image. Figure 2.5 shows how a one-dimensional profile is made with UOT. When the insonified volume passes through a region with absorption higher than its surroundings, the amount of tagged photons detected is reduced, as tagging is dependent to the optical fluence inside the insonified volume, causing a dip in the signal. This can then be repeated by shifting the position of the US to form a two-dimensional image.

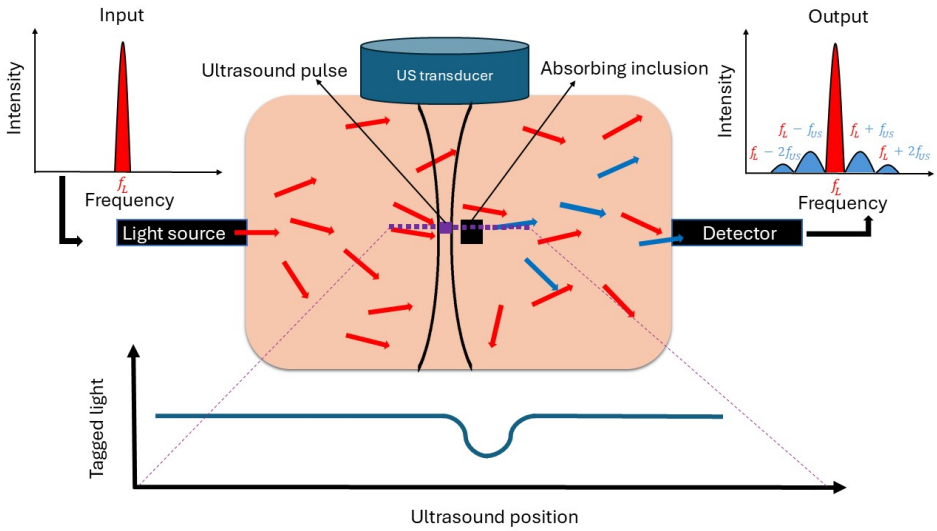

Figure 2.5: Principle of UOT. Light of frequency f_L (red arrows) is sent into the tissue. The light which passes through the US pulse, of frequency f_{US} (purple square), has some probability of getting frequency shifted or tagged (blue lines) to a frequency $f_L \pm nf_{US}$. As the amount of tagged light is a function of local fluence, when the US pulses passes through an optically denser region of the tissue, the amount of tagged light decreases. An example of a one-dimensional signal profile is shown in the lower half of the figure, showing a dip in the amount of detected tagged light when the ultrasound pulse in focused on an absorbing inclusion.

Chapter 3

Methods

This section describes the experimental setup, key components and procedures used to carry out the measurements. It includes an overview of the detection scheme and its operating principles, details regarding the phantoms, and a description of the two imaging approaches used to obtain the UOT images.

3.1 Photorefractive crystals

The detection scheme used in the thesis is based on photorefractive (PR) crystals, which uses PR holography to detect tagged photons. The PR effect is a non-linear effect that induces a local change of refractive index as a response to inhomogeneous illumination. This effect arises due to a change in the electric field within the crystal caused by the redistribution of charge carriers affected by photoexcitation. The movement of large amounts of carriers causes a refractive index modulation, and the reestablishment of local electric fields due to carrier movement is not immediate [37], but governed by a characteristic PR response time, denoted by τ_{PR}. It is the time until a steady-state is achieved in the crystal after a change in irradiation. This can be used to record a temporary[1] hologram on the crystal, which can be used for the diffraction of light. Due to the τ_{PR} of the crystals, the holograms that can be recorded are only those that move slower than the response time of the crystal. As a self-adaptive wavefront interferometry technique, this approach allows the use of large-area single element detectors [37]. All speckles that come from the medium being imaged can be integrated into a single detector through holography, allowing a higher signal-to-noise ratio (SNR) to be achieved [16].

[1] This can be reversed by illuminating the crystal with spatially homogeneous light

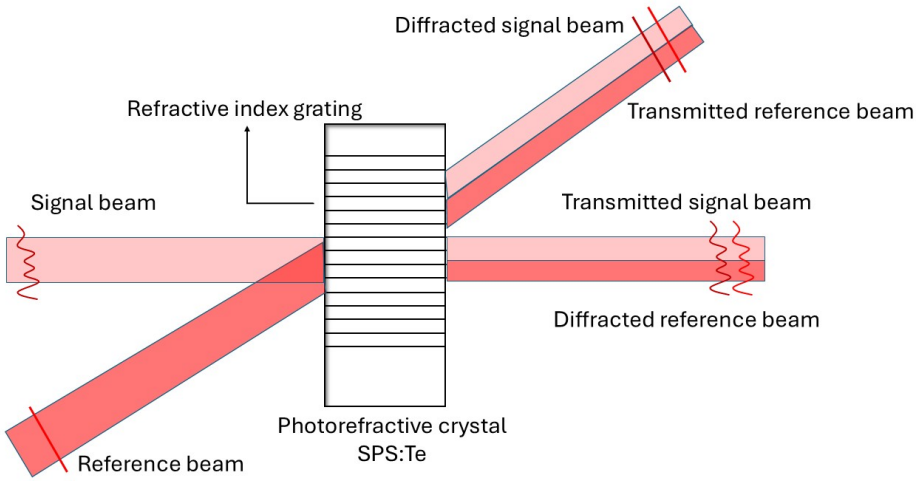

Figure 3.1: Illustration of two-wave mixing in a PR crystal. The interference between the signal, which is the speckle pattern emerging from the medium, and reference beams (set at the frequency of untagged light) induces a refractive index grating within the crystal. After propagation through the grating, the transmitted signal beam and the diffracted reference beam have matched wavefronts, enabling constructive interference and detection of the acousto-optic signal. Inspiration taken from [37].

When the reference beam, set at the frequency of untagged light in the setup used in this thesis, and the signal beam is incident on the PR crystal, their interference creates a refractive index grating. Through a process known as two-wave mixing, the reference beam is diffracted by this grating and acquires matched wavefronts (and direction) as the signal beam [16, 17, 37]. Figure 3.1 illustrates how two-wave mixing occurs through a PR crystal. Now spatially coherent, they can constructively interfere. As a consequence, phase modulation caused by the ultrasound-light interaction can be converted into a modulation of intensity.

The extraction of the acousto-optic signal is fundamentally limited by the τ_{PR} of the crystal. US has a propagation speed of 1540 m/s or 1.54 mm/µs in biological media, whereas typical PR crystals[2] exhibit $\tau_{PR} \sim 10$ ms. Consequently, the crystal cannot follow the rapid temporal variations associated with the propagation of an US pulse, meaning that if the reference beam is set at the frequency of the modulated light, the hologram will not be able to capture this information as it is too slow to respond to the passage of the US pulse. To address the limitation, the reference beam is tuned at the frequency of the unmodulated light. A portion of the illumination light is used as the reference beam, and the hologram is recorded prior to the emission of the US pulse, implying the interference takes at the frequency of unmodulated light. In the

[2]Including the one used in the setup mentioned in this thesis

absence of the US pulse, the reference beam and signal beam interfere constructively, producing a maximum detected signal. When the US pulse propagates through the sample, it induces a frequency shift in a fraction of the scattered light. This frequency shift disrupts the established interference condition, causing a decrease in the detected signal. When the interaction takes place at an absorbing region, fewer photons are tagged, and the level of unmodulated light remain relatively unchanged. Therefore, the presence of absorbing features can be inferred from variations in the detected intensity.

Here, the detection of modulated light happens indirectly through a measurement in the decrease of unmodulated light. This is different from techniques like spectral hole burning, in which the tagged photons are detected directly by passing the signal beam through a highly selective and narrow-band optical filter. There is another characteristic quantity of a PR crystal, which is the PR gain. It represents the amplification of the signal beam, equal to the ratio between the signal beam power with and without a reference beam [37]. It has units of m^{-1}. A primary source of noise in PR detection is beam fanning, a parasitic effect in which the reference beam alone generates refractive index gratings, leading to unwanted diffraction and signal distortion. To mitigate this effect, the PR crystal is operated in a negative gain configuration (attenuation regime), which reduces beam fanning and improves measurement stability [47], as opposed to a positive gain configuration (amplification regime).

3.2 Phantoms

Before imaging biological tissue, experimental techniques must be validated on phantom samples. These can range from *ex vivo* animal tissue samples to purpose built synthetic materials designed to mimic optical and acoustic properties of biological tissue. In this thesis, two types of synthetic phantoms were fabricated to test the two imaging approaches. The two types of phantoms were made from agar-intralipid (AgI) mixture and styrene-ethylene / butylene-styrene (SEBS) copolymer in mineral oil. The AgI phantoms were prepared following the procedures described in [47, 48], while the SEBS phantoms were fabricated according to [49]. Figures 3.2a and 3.2b show the SEBS phantoms and their inclusions prior to the addition of the final layer.

Two different AgI phantoms were prepared, each containing a circular absorbing inclusion made using India ink. These inclusions were made to mimic localized absorption in tissue. The two phantoms differed in both thickness and size of the inclusion.

The first phantom, referred to as AgI1, had a thickness of 15 mm and contained a relatively large inclusion. The exact size of the inclusion for AgI1 could not be deter-

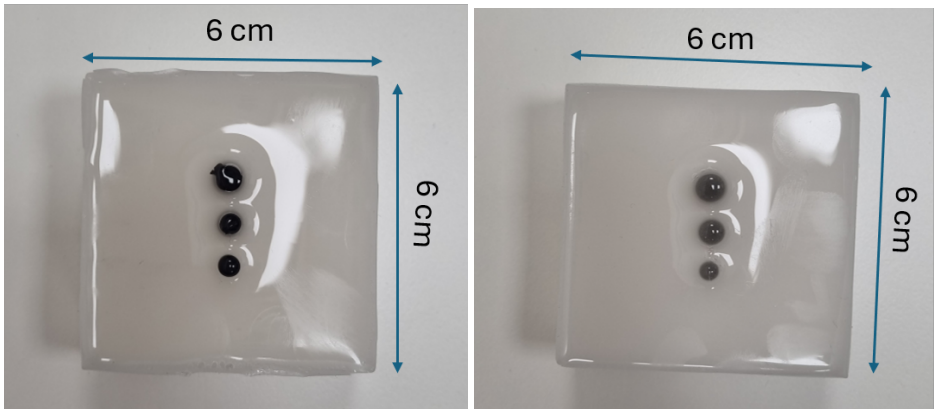

(a) Top down view of SEBS1 showing the three inclusions before the background material was put in.

(b) Top down view of SEBS2 showing the three inclusions before the background material was put in.

Figure 3.2: Images of SEBS phantoms.

mined due to the diffusion of the ink during storage. The second phantom, AgI2, had a thickness of 30 mm and contained a well defined inclusion with a diameter of 4 mm. Both AgI phantoms had dimensions of 5 cm $\times$ 5 cm as their length and breadth.

There were also two types of SEBS phantoms that were fabricated. Each contained three approximately cylindrical inclusions of different sizes, separated by approximately 5 mm, with radii $r_1 = 1.70$ mm, $r_2 = 2.25$ mm and $r_3 = 2.80$ mm. These correspond to having a cross-sectional areas of $\approx$ 9 mm^2, 16 mm^2 and 25 mm^2, respectively. Both phantoms had identical background material but differed in the type and size of inclusions. The first phantom, SEBS1, contained inclusions composed of the background material mixed with graphite, resulting in high absorption contrast. The other SEBS phantom, SEBS2, contained inclusions composed of the background material with an increased concentration of the same absorber used in the background, resulting in a lower absorption contrast compared to SEBS1. During the fabrication of SEBS1, one inclusion partially melted, forming a large inclusion of unknown dimensions. This can be seen in chapter 5 in figure 5.2a. Both SEBS phantoms had dimension of 6 cm $\times$ 6 cm $\times$ 3 cm.

Table 3.1 shows the reduced scattering and absorption coefficients for the different phantoms. For the AgI phantoms, these values were verified following the procedure described in ref.[50], whereas for the SEBS phantoms, they were measured using photon time-of-flight spectroscopy (PTOFS). The absorption coefficient of the AgI phantoms was not known accurately as PTOFS measurements could not be carried out on them, but their μ_a were seen to be lower than that of the SEBS phantoms. This was qualitatively noticed during measurements, as higher illumination intensity was required to obtain a detectable signal in the SEBS phantoms.

Table 3.1: Reduced scattering coefficients and absorption coefficients of the AgI and SEBS phantoms.

	AgI1	AgI2	SEBS1	SEBS2
μ_s' (cm^{-1})	10	8.5	8.5	8.5
μ_a (cm^{-1})	-	-	0.04	0.04

3.3 Imaging approaches

In this thesis, two approaches of conducting UOT are investigated experimentally: focused waves and FT-UOT. The following sections describe these techniques and their methodology respectively.

3.3.1 Focused regime

Focused waves, hereafter referred to as the focused regime, represent the most common and direct approach of performing UOT measurements. Here, acousto-optic interaction is achieved by insonifying the medium (phantom in this case) with a spatially localized US pulse. As the pulsed focused wave propagates, the tagged photon flux can be monitored over time. This enables measurements to be depth-resolved through a direct time-to-position mapping. By performing a line by line scan, a two-dimensional image can be then reconstructed. A schematic of this process is shown in figure 3.3. Lateral resolution is governed by acoustic diffraction [37], making the focal spot size on the order of a few acoustic wavelengths. It is also influenced by the effective aperture of the transducer (number of elements activated to generate a pulse), which determines the width and spacing of successive US pulses. The axial resolution is connected to the temporal duration of the pulse, hence the spatial length of the pulse along the direction of propagation.

During acquisition for focused regime, each element is activated sequentially, with the corresponding signal recorded to form a single line of the image. This process is repeated for all elements, resulting in the full reconstruction of the image. The acquisiton can be performed multiple times to enable signal averaging and to improve the SNR.

3.3.2 Fourier Transform Ultrasound Optical Tomography

In FT-UOT, also referred to as Fourier transform acousto-optic tomography (FT-AOT), is an alternative imaging approach to UOT. In this configuration, the entire medium (or a large part of it) is insonified using amplitude modulated US waves. The amplitude modulation is used to create spatial structuring of the pressure field.

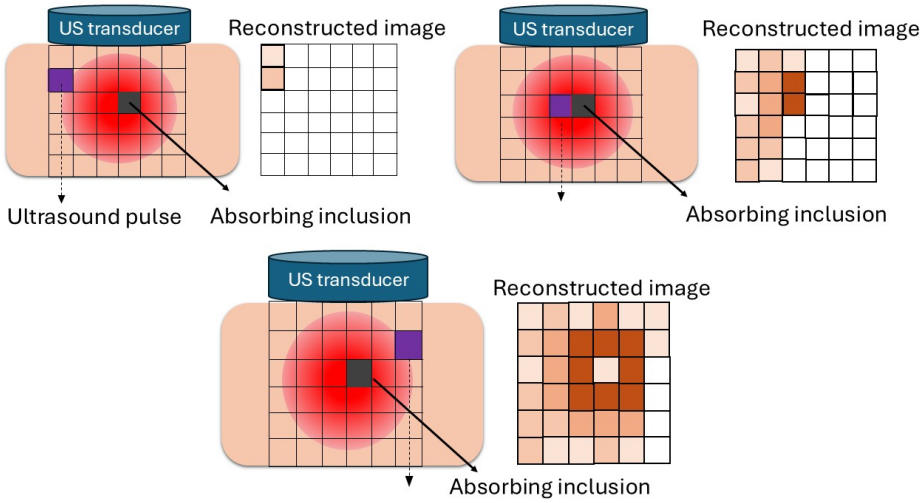

Figure 3.3: Visualization of image reconstruction using a focused US pulse. As the US pulse propagates through the medium, it generates a time-dependent acousto-optic signal that is recorded and used to reconstruct a single line of the image. By sequentially activating different elements of the transducer, the US focus is laterally displaced, allowing successive lines to be acquired and forming a two-dimensional image of the phantom.

As the structured US field propagates through the medium, the tagging efficiency of the photon flux is higher at spatial locations where the US intensity is higher as given by the spatial frequencies of the US field, allowing measurements through Fourier encoding [51–53]. A two-dimensional image is then reconstructed by acquiring multiple measurements through different spatial modulation patterns to obtain various Fourier components, and then performing an inverse Fourier transform. A schematic of this process is shown in figure 3.4. The lateral and axial resolutions are decided by the spatial frequencies along the two different spatial directions, which are denoted by x and z in this case. The lateral structuring is controlled by the transducer array, with spatial frequencies defined by harmonics of the fundamental frequency set by the width of a single transducer element. The axial structuring is attained through introducing periodic temporal delays to the transducer, which translates into a spatial modulation along the axis of US propagation. By varying both the harmonic components, different Fourier components of the image are captured.

An important advantage of FT-UOT is that the use of long pulses (temporally long but spatially separated) increases the tagging volume, improving signal strength in comparison to the focused regime. Spatial resolution is preserved through the modulation of US rather than geometric confinement to a small focused spot. This comes at the cost of requiring multiple acquisitions to sufficiently sample the Fourier space.

To conduct FT-UOT, either the full transducer array or a subset of its elements can

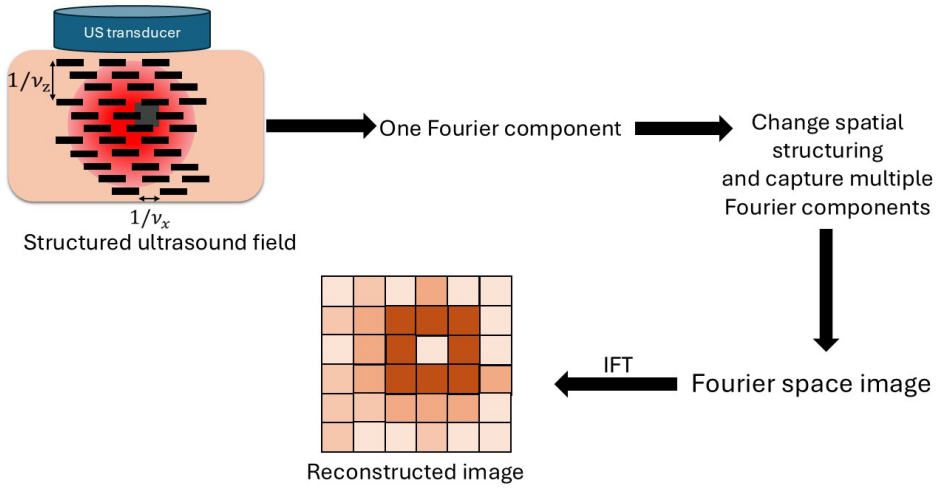

Figure 3.4: Visualization of image reconstruction using FT-UOT. A spatially structured US field is used to generate an acousto-optic signal in which spatial information is encoded in the Fourier domain. For each pair of spatial frequencies (ν_x, ν_z) a temporal signal is recorded and processed to obtain a single Fourier component of the image. This procedure is repeated for multiple spatial frequency pairs to sample the desired Fourier space. A two-dimensional image of the phantom is then reconstructed by applying an inverse Fourier transform.

be used to generate the spatial structuring of the US field. The fundamental structuring frequency in the lateral direction is given by $\nu_{x_0} = 0.02$ mm^{-1} and in the axial direction it is defined as $\nu_{z_0} = 1/c_s T_0 = 0.03$ mm^{-1}, where T_0 is the user-defined temporal modulation and c_s is the speed of sound in the medium. In the measurements conducted in this work, the modulation period was set to $T_0 = 20$ µs.

To reconstruct an image for FT-UOT, the temporal trace associated with each pair of spatial frequencies (ν_x, ν_z) is recorded. After averaging, it is multiplied by a demodulation function [52]. The demodulation function is defined as,

$$h_m(t) = \exp(-2\pi i f t), \tag{3.1}$$

where $f = c_s \nu_z$. Each Fourier component is then obtained by integrating over acquisition time T.

3.4 Experimental set-up

The experimental setup consists of an optical illumination system, an ultrasonic excitation system, and a PR detection scheme. An overview of the setup is shown in figure 3.5. The optical source is a master oscillator power amplifier (MOPA) system

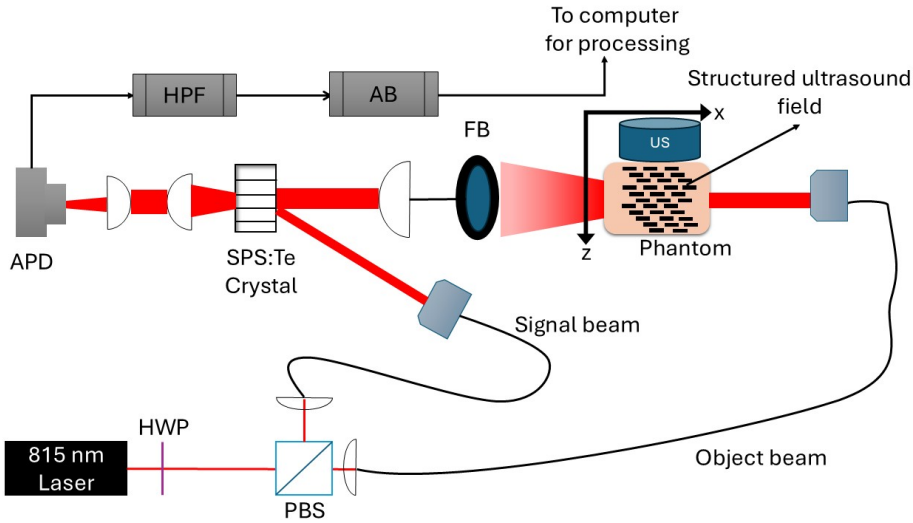

Figure 3.5: Experimental setup using PR holography. HWP- half-wave plate, PBS- polarizing beam splitter, FB- fiber bundle, APD- avalanche photo-diode, HPF- high pass filter, AB- acquisition board.

(TOPTICA Photonics TA Pro), delivering single longitudinal mode emission at a wavelength of 815 nm with an output power of 2.5 W in continuous-wave operation. The object beam is coupled into a multimode optical fiber with a core diameter of 100 µm for ease of handling and alignment. At the fiber output, a zoom system is used to expand the beam to approximately 2 cm in diameter, enabling uniform illumination of apart of the phantom. The ultrasonic transducer placed perpendicular to the axis of light propagation, imaging the *x*-*z* plane. The transducer produces US waves by sending electrical pulses into piezoelectric crystals, which expand and contract rapidly to produce mechanical vibrations. It is placed on top of the phantom with adequate US gel applied to ensure proper contact between the transducer and phantom. The AgI phantoms were placed in a water tank, as they were too brittle to be placed in direct contact with the US transducer. US is generated using a 192-element linear array transducer (SuperSonic Imagine Aixplorer SL10-2 probe), each with a width of 0.2 mm. As will be discussed later in section 5, the transducer is not designed to emit complex US patterns, like the ones required for FT-UOT. This can sometimes lead to poor structuring of the US fields, leading to poorer imaging quality. Therefore to avoid overheating or damaging the transducer, the voltage used for FT-UOT was set to 15 V, compared to 50 V for the focused regime.

The transmitted light is collected using a large-core fiber bundle with a numerical aperture of 0.2, coupled with a high-aperture lens of focal length 5 cm. The collected signal is focused onto a SPS:Te ($Sn_2P_2S_6$ doped with 1% Te) crystal 8 mm × 8 mm × 8 mm in dimensions, where two-wave mixing enables selective amplification of the

ultrasonically tagged photons. The crystal exhibits PR gain of approximately $\tau_{\mathrm{PR}} \approx 2\ \mathrm{cm}^{-1}$. The setup is placed in transmission geometry.

The signal from the crystal is then imaged onto a silicon avalanche photodiode (APD) with an active diameter of 1.5 mm and a conversion factor of 1.5 V/μW. Imaging is achieved through a two-lens system with focal lengths of 5 cm and 1 cm, respectively, ensuring efficient collection of the modulated optical signal. Finally, the electrical output from the APD is passed through a high-pass filter to remove the parasitic continuous-wave contribution before being recorded using a digital acquisition board. This enables isolation and analysis of the ultrasonically tagged photon signal.

Chapter 4

Simulations

The original plan for this thesis was to investigate the FT-UOT and its viability experimentally. However, due to unseen circumstances, the experiments could not be carried out initially within the planned time frame. As a result, a pivot was made to adopt a simulation based approach. Experimental measurements were later successfully performed, and the results are discussed in the chapter 5. As existing simulation models were intended for a small localized volume of US, simulating FT-UOT presented a challenge. To the best of the author's knowledge, simulations involving US present in a larger volume to simulate FT-UOT, mostly remain unexplored.

To develop a simulation for FT-UOT, two approaches were considered: probabilistic models based on Monte Carlo [42, 44, 54–56] methods and analytical models based on the diffusion equation [57–59] (an approximation of the radiative transfer equation).

Monte Carlo methods are considered the gold standard in light propagation and UOT simulations for complex media. However, they are very computationally expensive and time consuming as they simulate the movement and interaction of every photon with an acoustic wave in a scattering medium. In these models, the acousto-optic interaction is modelled using the two coherent mechanisms outlined in section 2.4.1. These mechanisms are used to compute the modulated optical path lengths, hence the modulated phase [16, 44, 60]. This calculation of the accumulated phase is then repeated for every photon path for a small, localized US volume. Extending this approach to FT-UOT would be particularly challenging and computationally unfeasible[1], as the tagging volume in FT-UOT is significantly larger compared to the focused US regime.

[1]The memory required to store the accumulated path lengths for all photon trajectories for a large and spread out tagging volume would exceed the available resources.

In contrast, analytical models based on the diffusion equation are much faster to execute computationally, and more realistic to implement in the given time frame. Although limited by approximations, they are capable of providing valuable insight and information. However, most analytical models identified during literature review were restricted with respect to the goal of simulating FT-UOT. For example, some models only focused on the autocorrelation function of the tagged field [43, 61, 62], while others looked at homogeneous media [57] or focused US volumes.

The model that has been used in this work, based on diffusion equation, a perturbative approach, and mean photon path lengths, is discussed briefly in the next section, along with its application to simulate FT-UOT.

4.1 The idea

The formation of a two-dimensional image using FT-UOT was introduced by Bocoum et al. [52][2]. Building on the mathematical framework established in this work, the idea was to simulate FT-UOT with the analytical model mentioned below.

Both mathematical models are described briefly and how they are combined to create the simulation. For finer details regarding the models, the reader is referred to ref.[52, 59].

The model considers an inhomogeneous slab of thickness s, with $\mu_s' = 10\ \mathrm{cm}^{-1}$ and $\mu_a = 0.04\ \mathrm{cm}^{-1}$. The point source is located at $z_0 = 1/\mu_s'$, ensuring the validity of the diffusion approximation. The slab is divided into 8000 voxel, 20 along each spatial dimension.

The solution for the steady-state diffusion equation for an isotropic point source for a homogeneous slab is established in the literature [59, 63], and is given by the Green's function:

$$\begin{aligned}\Phi_h(\vec{r}) &= G(\vec{r}, \vec{r}_s) \\ &= \frac{1}{4\pi D} \sum_{m=-\infty}^{m=+\infty} \frac{\exp\left(-\mu_{eff}\sqrt{\rho^2 + (z - z_m^+)^2}\right)}{\sqrt{\rho^2 + (z - z_m^+)^2}} - \frac{\exp\left(-\mu_{eff}\sqrt{\rho^2 + (z - z_m^-)^2}\right)}{\sqrt{\rho^2 + (z - z_m^-)^2}}.\end{aligned} \tag{4.1}$$

where the h subscript denotes homogeneous, $\vec{r_s} = (x_s, y_s, z_s)$ is the location of the point-like isotropic source, $\mu_{eff} = (\mu_a/D)^{1/2}$, $D = 1/3(\mu_s' + \mu_a)$,

[2] See Chapter 3

$\rho = \left((x-x_s)^2 + (y-y_s)^2\right)^{1/2}$; z_m^+ and z_m^- denoting the z coordinates for virtual positive and negative sources respectively. The summation over m includes virtual point sources that are added on either side of the boundary of an infinite homogeneous medium, with $m = 0$ being the real source; + and - are the positive and negative sources, respectively.

The mean photon path lengths in a voxel i can be shown to be

$$\langle l_i \rangle = \Delta V \frac{G(\vec{r_d}, \vec{r_i})\, G(\vec{r_i}, \vec{r_s})}{G(\vec{r_d}, \vec{r_s})}, \tag{4.2}$$

where $\vec{r_i}$ is the voxel in question and $\vec{r_d}$ is the detector location [59].

There are two major assumptions made in this model. First, the probability that a photon is tagged is constant per unit path length it travels in the region with the US pulse. Second, photon cannot be tagged more than once in a voxel. The probability of tagging per unit path length covered in a region with US is indicated by the parameter κ. For the focused US regime, it is defined as

$$\kappa(\vec{r}) = \begin{cases} \kappa > 0, & \text{if } \vec{r} \text{ is inside the voxel with the US pulse ;} \\ 0, & \text{everywhere else.} \end{cases} \tag{4.3}$$

This is the quantity that is of interest, as it will be changed to account for spatially structured tagging. The tagged fluence[3] for a homogeneous slab is then expressed by

$$\Phi_h^{k,tag} = \Phi_h \kappa \langle l_k \rangle , \tag{4.4}$$

when the tagging occurs in voxel k.

The slab also consists of two inhomogeneities, which have a higher absorption coefficient than their surroundings. These inhomogeneities have additional absorption, represented by $\delta\mu_a$, and are called absorption perturbations. Using a perturbative approach with the Rytov approximation[4], the fluence in an inhomogeneous slab can be expressed as:

$$\Phi_{pert} = \Phi_h \exp\left(-\sum_{i=1}^{N} \delta\mu_{a,i} \langle l_i \rangle\right), \tag{4.5}$$

where the summation is over all voxels and $\delta\mu_a > 0$ for a voxel with inhomogeneity.

[3] Fluence of the frequency shifted light.

[4] $\langle l_i^n \rangle = \langle l_i \rangle^n$

The tagged fluence for an inhomogeneous medium is not so easily explained. A distinction must be made between the photons travelling directly from source to detector, expressed equation (4.4) and those that are tagged in a voxel k before reaching the detector. The latter is described by:

$$\Phi_{pert}^{k,tag} = \Phi_{h}^{k,tag} \exp\left(- \sum_{i=1}^{N} \delta\mu_{a,i} \left\langle l_i^{(k)} \right\rangle \right). \tag{4.6}$$

The distinction is made by the term $\left\langle l_i^{(k)} \right\rangle$, which expresses the average path length of a photon in voxel i when it was tagged in voxel k, unlike equation (4.2) which only expresses the average path length of a photon in voxel i.

The UOT signal is defined as the ratio between transmittance of the first order shifted light, $T_1^{(k)}$[5], and the zero order (unshifted) light, T_0 ;

$$\frac{T_1^{(k)}}{T_0} = \kappa \left\langle l_k \right\rangle \exp\left\{ - \sum_{i=1}^{N} \Delta\mu_{a,i} \left[\left\langle l_i^{(k)} \right\rangle - \left\langle l_i \right\rangle \right] \right\}. \tag{4.7}$$

In the FT-UOT framework [52], the signal acquired from a single measurement during a FT-UOT measurement i is defined as

$$S_i = \int M_i(\vec{r})\, I(\vec{r})\, dV, \tag{4.8}$$

where $M_i(\vec{r})$ is the tagging function, which depends on the type of detection scheme and the shape of the US pulse. $I(\vec{r})$ is the image that would be obtained through the focused regime, which depends on the local fluence and local optical properties.

For detection schemes such as PR crystals and spectral hole burning, which are temporally sampled signals [52], the complex tagging function in two dimensions can be shown by:

$$M_i(x, z) \propto j \ \exp(-2\pi j(\nu_x x + \nu_z z) + j\phi). \tag{4.9}$$

Having established the mathematical requirements of FT-UOT and the analytical model, we can now discuss how to combine the two. To incorporate spatially structured tagging into the analytical model, equation (4.9) is used to define $\kappa(\vec{r})$ for FT-UOT as

$$\kappa(\vec{r}) = \kappa_0 \exp\left(-2\pi j \left\{\nu_x x_k + \nu_z z_k\right\}\right), \tag{4.10}$$

where κ_0 is a constant, ν_x and ν_z are the spatial frequencies of the US in the x and z direction,respectively. Instead of $\kappa(\vec{r})$ being confined to a single voxel, as expressed by

[5]When the tagging occurs in voxel k.

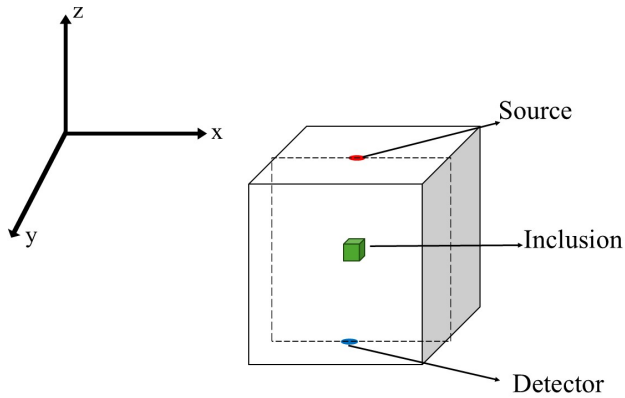

Figure 4.1: Geometry of the simulation. The source is located at $(x_s, y_s, z_s) = (0, 0, 60)$ mm. The detector is located at $(x_d, y_d, z_d) = (0, 0, 0)$ mm. The inclusion is located at $(x_a, y_a, z_a) = (4.5, 1.5, 28.5)$ mm. The dashed lines indicate the plane $x - z$ plane which is being imaged.

equation (4.3), it is now spatially modulated across the entire medium . The resulting signal from one measurement, S_i becomes

$$S(\nu_x, \nu_z) = \sum_{k=1}^{N} \overbrace{\kappa_0 \exp\left(-2\pi j \left\{\nu_x x_k + \nu_z z_k\right\}\right)}^{M_i(\vec{r}) - \text{Tagging function}} \underbrace{\langle l_k \rangle \exp\left\{-\sum_{i=1}^{N} \delta\mu_{a,i} \left[\left\langle l_i^{(k)} \right\rangle - \langle l_i \rangle\right]\right\}}_{I(\vec{r})}. \quad (4.11)$$

The summation of k is performed over all voxels as in FT-UOT all voxels are tagged simultaneously. By varying (ν_x, ν_z), multiple measurements are acquired to build the Fourier grid, and consequently the final image through an inverse Fourier transform of the grid.

4.2 Simulation results and analysis

An important point to note is that the reconstruction of the image using FT-UOT requires prior computation of $I(\vec{r})$. In this work, this is built using the analytical model as mentioned in the previous section. After $I(\vec{r})$ is built, only then can the complex tagging function be applied to simulate a signal acquisition. Figure 4.1 shows the geometry of the simulation. The source is located at $x = 0, y = 0$ and $z = 60$ mm. The detector is located at $x = 0, y = 0$ and $z = 0$ mm. The slab contains one absorbing inclusion, three voxels wide in all three directions. It is centered at

$(x_a, y_a, z_a) = (4.5, 1.5, 28.5)$ mm. It has an additional absorption of 0.05 mm^{-1} relative to the background.

Figures 4.2 show the main results of the simulation. Figure 4.2a shows the mean path length of photons $\langle l_k \rangle$ (equation 4.2) in each voxel in the *x*-*z* plane. This distribution is independent of US involvement and reflects the optical sensitivity of the measurement. It has the highest sensitivity along the path that connects the source and the detector, falling off toward the sides. The location of the source ($x = 0$ and $z = 60$ mm) and detector ($x = 0$ and $z = 0$ mm) can be seen through the voxels with high intensity. Figure 4.2b is the ground truth image, this is what the simulation is trying to recover. It shows the location of the inclusion in the *x*-*z* plane. Figure 4.2c is the image obtained using the simulation for the focused US regime, done through equation 4.7 . The inclusion can be seen as a dip in the signal intensity, highlighted by the red-dashed lines. This is the $I(\vec{r})$ used for the reconstruction of the FT-UOT image.

The central result of the simulation is displayed in figure 4.2d. It is the image reconstructed after the inverse Fourier transform of all the measured signals S_i, which is done through equation 4.11. The result demonstrates that FT-UOT is, in principle, capable of recovering images comparable to those obtained via the focused US regime, showing a strong theoretical backing for FT-UOT.This simulation could also be used to see which spatial frequencies will be better to use for FT-UOT depending on the size of the inclusion. Figure 4.2e is the relative contrast map. It isolates the signal caused purely by the inclusions, i.e, what fraction of the tagged signal changed compared to a medium with no inclusions. Negative values indicate the location of the absorbers as they reduce the tagged signal. Figure 4.2f shows the corresponding Fourier domain representation. The signal is concentrated near the DC component $(m = 0, n = 0)$, reflecting the smooth spatial structure of the object. Each sampled pair, (ν_x, ν_z), corresponds to a pixel in the plot. Appendix A shows the results of the simulation for two inclusions and images reconstructed in the *x*-*y* plane at $z = 28.5$ mm for one and two inclusions.

4.3 Limitations

It is important to mention that these results cannot be compared to experimental results discussed in chapter 5. The simulation conditions are highly idealized and rely on approximations that are unable to fully capture the complexity of the experimental set-up used in this thesis. The simulation serves to validate the theoretical framework of FT-UOT and to explore the sensitivity of the methods to absorption inhomogeneities under idealized conditions. The simulation does not account for the

PR detection[6], experimental losses[7], higher harmonics of the tagged light, divergence and diffraction of acoustic waves, and any explicit noise sources.

[6]Does not consider speckle or coherence effects, which are used PR detection.

[7]Such as, fiber coupling efficiency,detector quantum efficiency and optical losses at interfaces.

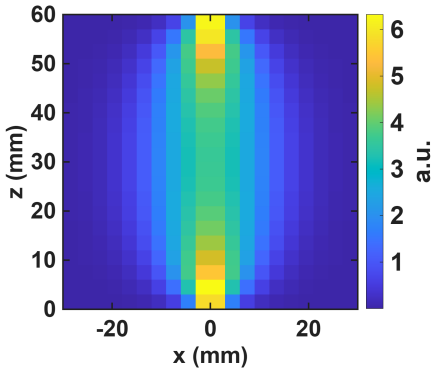

(a) Mean path length in each voxel.

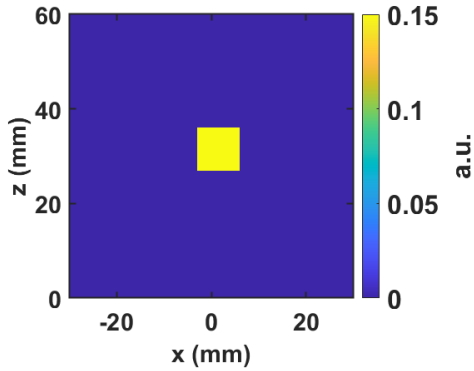

(b) Ground truth image for one inclusion case.

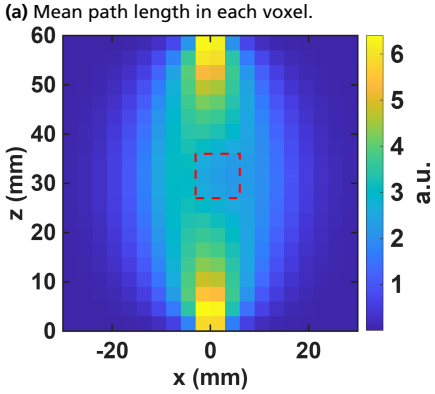

(c) Image constructed through focused regime.

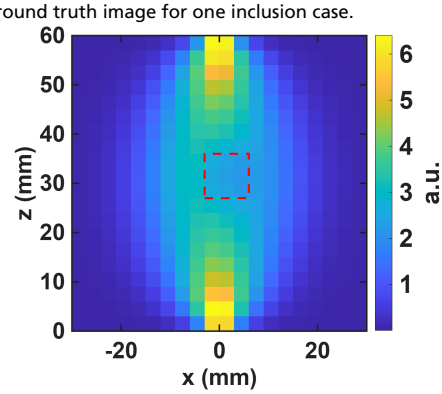

(d) Image reconstructed through FT-UOT.

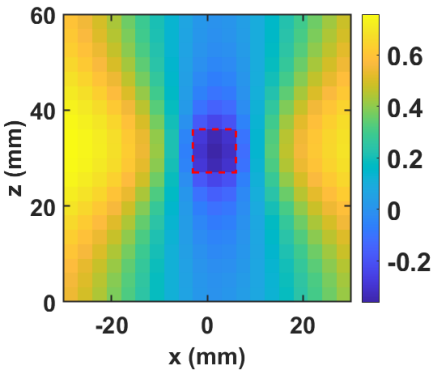

(e) Relative contrast map.

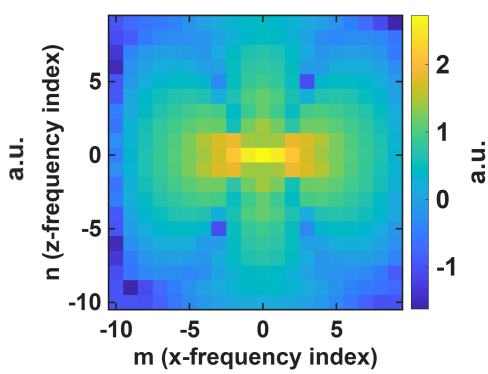

(f) Fourier plane log|S(m,n)|.

Figure 4.2: Results for the one inclusion case for the focused regime and FT-UOT. The inclusion is marked with red-dashed lines to indicate their location in the medium.

Chapter 5

Results and discussions

This section presents the results of the experiments performed at the Langevin Institute in Paris. The images were taken on two types of tissue-mimicking phantoms, AgI and SEBS in mineral oil, on the PR detection set-up (see chapter 3 for details). The phantoms were imaged in the focused regime as well as by using FT-UOT, and the results are then compared.

5.1 Results

Figure 5.1 presents images recorded with different US frequencies and SPLs. It illustrates how different US frequencies and SPLs impact the quality of a UOT image, and how choosing appropriate parameters is important so that maximum information can be retrieved. Figures 5.1a and 5.1b were obtained with an US frequency centered at 4 MHz with SPLs of 1 mm and 2 mm, respectively. Similarly, Figures 5.1c and 5.1d correspond to a center frequency of 3 MHz, with SPLs of 1 mm and 2 mm. Among these configurations, figure 5.1d shows the highest contrast, as indicated by its colour scale, while the minimum values remain consistent across all images. Both the visual quality and contrast suggested the combination of an US frequency of 3 MHz with a SPL of 2 mm provided optimal imaging performance for this system and phantom. Therefore, these parameters were used for the focused regime as well as FT-UOT images. These images were acquired using the AgI1 phantom, but similar results were observed for the other phantoms as well.

For direct and fair comparison, images from both techniques are presented under identical experimental conditions. The colour bars for the focused regime represent the AC voltage in mV, whereas FT-UOT images are shown in arbitrary units because

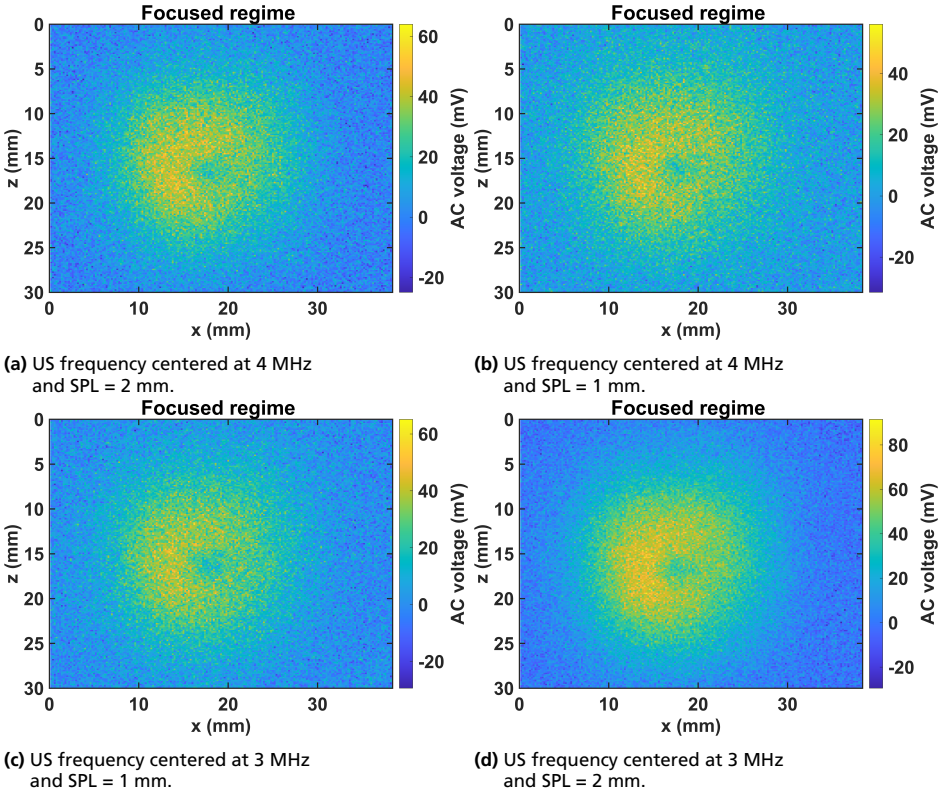

(a) US frequency centered at 4 MHz and SPL = 2 mm.

(b) US frequency centered at 4 MHz and SPL = 1 mm.

(c) US frequency centered at 3 MHz and SPL = 1 mm.

(d) US frequency centered at 3 MHz and SPL = 2 mm.

Figure 5.1: Focused regime images of AgI2 taken at different US frequencies and SPLs.

the reconstruction method only shows the relatively intensity. A single image acquisition is defined as the completion of one full imaging sequence. For the focused US regime, this corresponds to the sequential activation of all transducer elements across the imaging field. For FT-UOT, it corresponds to the capture of all desired Fourier components. The images shown are averaged over 500 acquisitions, unless otherwise mentioned. The spatial frequencies used for all FT-UOT images are $\nu_z = m\nu_{z_0}$ and $\nu_x = n\nu_{x_0}$, where $\nu_{z_0} = 0.033$ mm, $\nu_{x_0} = 0.026$ mm, $m \in [-10, 10]$ and $n \in [1, 10]$.

Figures 5.2a and 5.2b show SEBS1 images taken with an US frequency centered around 3 MHz, 2 mm spatial pulse width (SPL), focused at a depth of 15 mm in the image. The phantom is imaged through the 3 cm side, as insufficient signal was detected through the 6 cm side. The phantom was exposed to 110 mW/cm^2 with the reference beam on the PR crystal being 160 mW. Under these conditions, the focused regime image is much clearer; distinctly resolving two of the three inclusions. Only two of the three inclusions are visible as a result of the limited area of light collection,

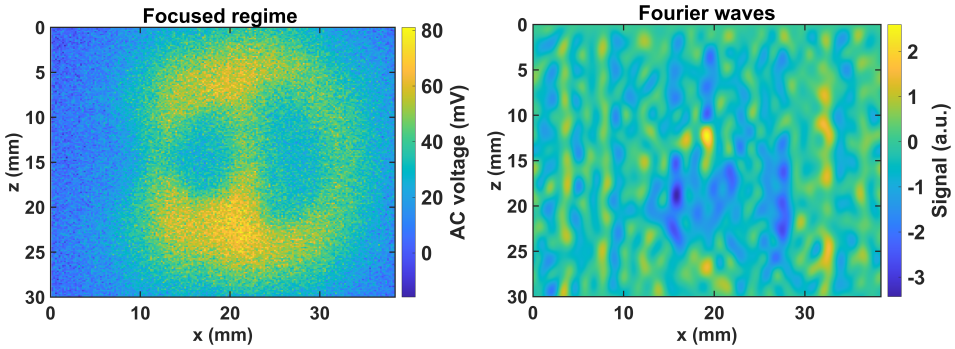

(a) Focused regime image of .

(b) FT-UOT image of SEBS1.

Figure 5.2: UOT images of SEBS1 with the Focused regime and FT-UOT, with US frequency centered at 3 MHz and SPL $= 2$ mm.

which limits the effective imaging area. In contrast, the FT-UOT image shows no particular features of the phantom. This is likely due to insufficient FT-UOT signal at the detector, caused by higher absorption of the SEBS phantom compared to the AgI phantoms (discussed later).

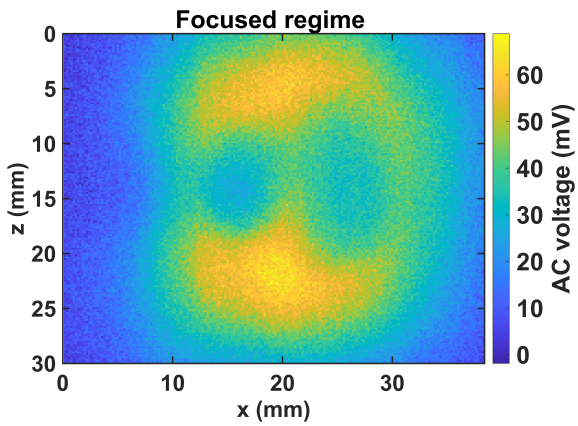

Figure 5.3: SEBS1 imaged through focused regime averaged 2000 times.

An image was acquired through the focused regime with 2000 averages to evaluate the effect of increased averaging. This result is shown in figure 5.3. The maximum signal value here is different from that previously shown in figure 5.2a, as the measurements were performed on different days, and the phantom position was slightly altered. Consequently, the *xz* plane that was imaged was slightly different. Nevertheless, the acquired image has a better contrast, which can be clearly seen. As the SNR is expected to scale as $\sqrt{N}$, where N is the number of acquisitions, this should increase image quality. However, considering diminishing returns and increased acquisition times, a decision was made to stick with 500 as the number of acquisitions to average.

Figures 5.4a and 5.4b show the UOT images of the SEBS2 phantom. Two of the three inclusions are clearly visible, the third was not being imaged due to the limited effective imaging region, as mentioned previously. When comparing the maximum signal from SEBS1 in figure 5.2a, a difference of approximately 20% can be observed. This can be attributed to the size and material of the inclusions being different. The inclusions in SEBS1 are larger and contain graphite, making it more attenuating than the inclusions in SEBS2. The highest signal intensity is observed in regions immediately above the inclusions. The smaller inclusion sizes in SEBS2 are reflected in the UOT image. However, the equivalent Fourier waves image does not show any particular features again, for this particular setup configuration. This is due to the same limitations discussed above, insufficient detected FT-UOT signal.

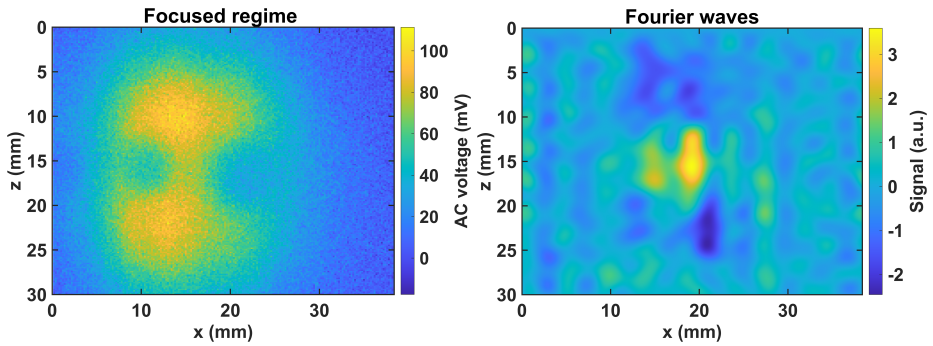

(a) Focused regime image of SEBS2.

(b) FT-UOT image of SEBS2.

Figure 5.4: UOT images of SEBS2 with the Focused regime and FT-UOT, with US frequency centered at 3 MHz and SPL $= 2$ mm.

The AgI1 phantom (single inclusion) was imaged through its 15 mm side. This was imaged using an incident intensity of 55 mW/cm^2. A lower intensity was chosen because the phantom is less absorbing (and scattering) and thinner, as higher intensities might saturate the APD. The reference beam power was set to 160 mW. The circular inclusion is clearly visible in the focused regime figure 5.5a, with an approximate diameter of 10 mm. The corresponding Fourier waves images, figures 5.5b and 5.5c also reveal the feature of the inclusion. The location and size of inclusion are similar for both techniques. However, the feature is not as circular as seen through the focused regime and exhibits some distortion. The difference between the two FT-UOT images is the number of transducer elements excited to generate the spatial structuring of the US waves. As described in chapter 3, the transducer has 192 elements, each being 0.2 mm wide. Figure 5.5b was obtained using elements $24 - 120$, which corresponds to half the available piezo-elements. Figure 5.5c was made using all elements of the transducer. Although activating all transducer elements does increase the tagging volume, it was observed that it leads to degradation of image quality from previous and current

experimental results. This is evident at $x \approx 26$ mm in 5.5c, where there appears to be a separation in the inclusion. The inclusion in figure 5.5b appears smaller because the transducer elements used are $24 - 120$, which correspond to 4.8 mm to 24 mm on the x-axis. This is the reason why the image is truncated at $x \approx 24$ mm.

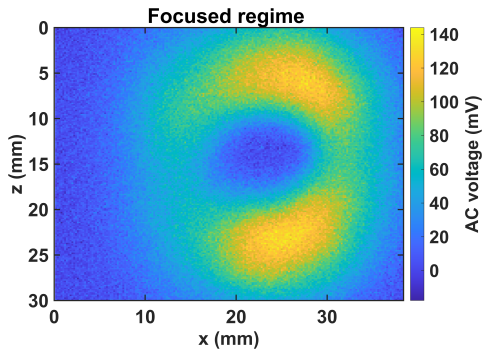

(a) Focused regime image of AgI1.

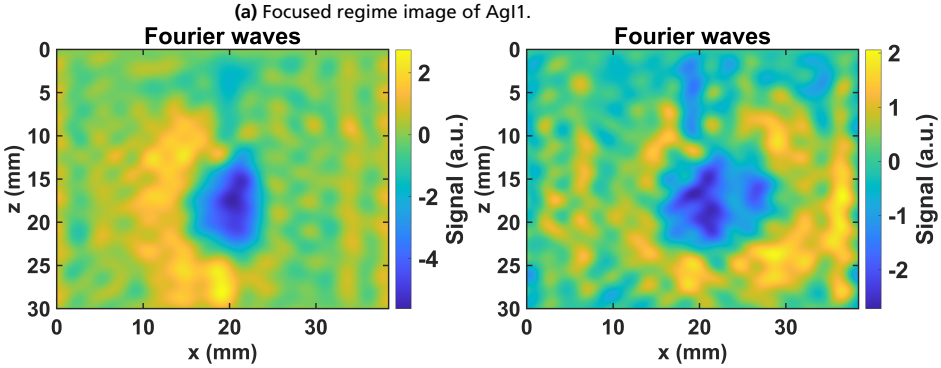

(b) FT-UOT image of AgI1 with transducer elements 24-120 excited.

(c) FT-UOT image of AgI1 with all transducer elements 1-192 excited.

Figure 5.5: UOT images of AgI1 with the Focused regime and FT-UOT, with US frequency centered at 3 MHz and SPL $= 2$ mm.

Using all the transducer elements is not ideal for imaging. This can be attributed to the fact that available US transducers are not designed for the emission of continuous complex US patterns, which is required to produce a spatially structured US pattern for FT-UOT. Driving all elements simultaneously to produce two-dimensional spatial structuring places excessive stress on the US transducer, leading to poorer quality structuring of the US. This is undesirable as it causes the loss of information due to Fourier components being encoded inaccurately. Therefore, careful selection of transducer elements is necessary to achieve reliable image reconstruction.

Figure 5.6 are the UOT images of the AgI2 phantom. It was imaged through its 3 cm side with the incident intensity of the laser being 110 mW/cm^2. The focused regime

image, figure 5.6a, shows a single circular inclusion with a diameter of approximately 4 mm. Figures 5.6b, 5.6c and 5.6d are the images acquired through FT-UOT. These were acquired using different subsets of active transducer elements. Figure 5.6b is acquired using elements $72 - 168$, centering the inclusion between the two ends of the transducer. The shape and size of the inclusion match the focused regime image, which can be seen at $x = 24$ mm. Figure 5.6c was taken using elements $96 - 192$, effectively imaging only the right half of the phantom. Here, also, the inclusion is visible at $x = 24$ mm. Figure 5.6d was obtained by using the left half of the transducer elements $1 - 96$. As expected, there is no indication of the inclusion. These results highlight the importance of transducer element selection in FT-UOT. Proper alignment between the active acoustic field and region of interest is essential for accurate image reconstruction.

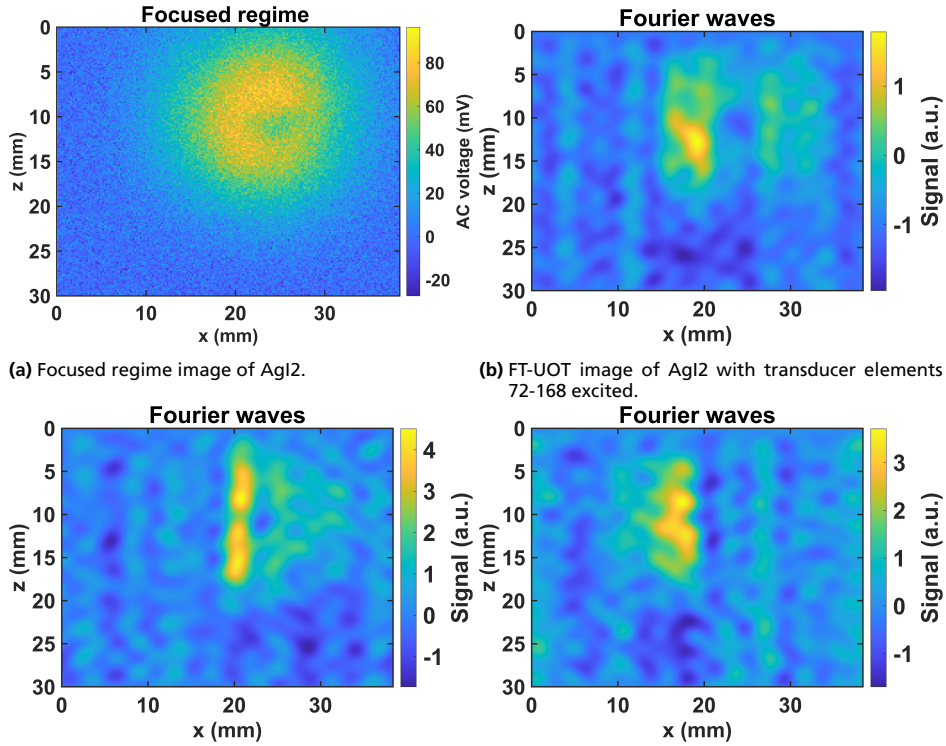

(a) Focused regime image of AgI2.

(b) FT-UOT image of AgI2 with transducer elements 72-168 excited.

(c) FT-UOT image of AgI2 with transducer elements 96-192 excited.

(d) FT-UOT image of AgI2 with transducer elements 1-96 excited.

Figure 5.6: UOT images of AgI2 with the Focused regime and FT-UOT, with US frequency centered at 3 MHz and SPL = 2 mm.

Initial FT-UOT images of the SEBS phantoms did not reveal any details about the inclusion, and this was suspected to be because of the lack of FT-UOT signal reaching the detector. To address this, one of the optical attenuators placed in front of the

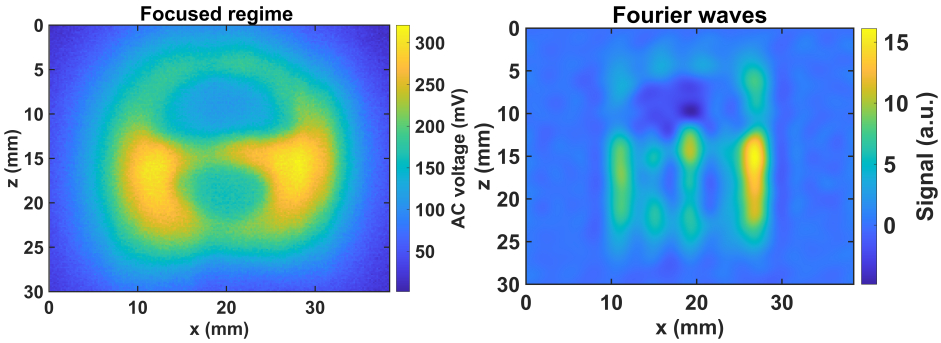

(a) Focused regime image of SEBS1 after removal of the attenuator.

(b) FT-UOT image of SEBS1 after removal of the attenuator.

Figure 5.7: UOT images of SEBS1 with the Focused regime and FT-UOT after removal of the attenuator, with US frequency centered at 3 MHz and SPL $= 2$ mm.

APD was removed. The resulting images are shown in figure 5.7. In addition, SEBS1 was rotated 90° relative to its previous orientation. The effect of the removal of the attenuator is visible for both the focused regime and Fourier waves. For the focused regime, the maximum signal increased by a factor of four, as seen on the colour scale in figure 5.7a. A corresponding increase is also seen in the FT-UOT image in figure 5.7b. The features of the inclusions in SEBS1 are visible through FT-UOT here. Although the FT-UOT reconstruction remain less well defined than the focused regime image, the location and general features are consistent between the two techniques.

This was also tested on SEBS2 and the results are shown in figure 5.8. The signal increased by a factor of five for the focused regime and approximately by an order of magnitude for FT-UOT. Inclusion features which were previously undetected in FT-UOT become visible after removal of the optical attenuator. Slight discrepancies in the z-axis are observed when compared to the focused regime, the overall features of the inclusions, showing two inclusions of slightly different sizes is preserved.

SNR of the images is evaluated by selecting a region of interest and creating a "smooth ideal" version of the image. Noise was defined as the standard deviation of the difference between the raw image data and the ideal reference. The SNR is therefore given by:

$$\text{SNR} = \frac{\text{mean (Smooth image)}}{\text{std (Fluctuations)}}. \tag{5.1}$$

This is done for both techniques, and the results of SNR as a function of number of acquisitions is shown in figure5.9. $\sqrt{N}$ progression is followed by the focused regime. FT-UOT initially does not follow this trend, although it begins to approach it after 50 acquisitions. The deviation is likely due to residual spatial artifacts caused by FT-UOT reconstruction, which might make this method of SNR calculation for FT-UOT not

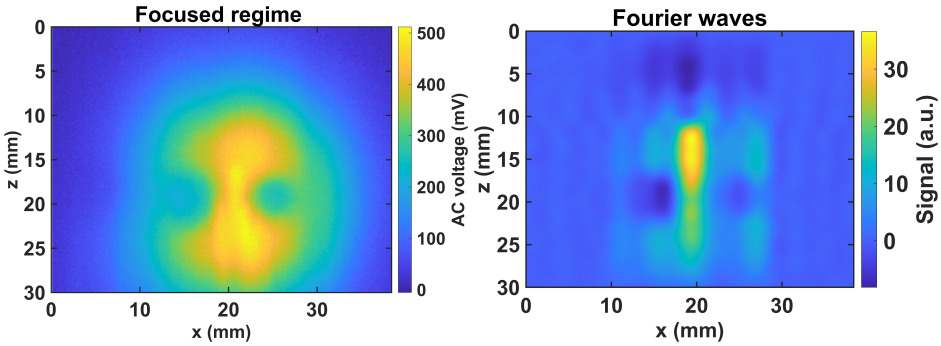

(a) Focused regime image of SEBS2 after removal of the attenuator.

(b) FT-UOT image of SEBS2 after removal of the attenuator.

Figure 5.8: UOT images of SEBS2 with the Focused regime and FT-UOT after removal of the attenuator, with US frequency centered at 3 MHz and SPL $= 2$ mm.

entirely accurate. This is further supported by the fact that the calculated SNR remain below unity, despite visible inclusion features. This suggests that the current SNR definition may not fully capture image quality in FT-UOT, and a more suitable metric may be required. The early "spiking" of the SNR for FT-UOT may possibly indicate that FT-UOT requires lesser averaging compared to the focused regime, but this is not entirely clear due to the SNR being less than unity.

All focused regime pictures presented above were made using the acquired raw data. In practice, images are often filtered to improve visual quality. Figure 5.10a shows the original raw data used to reconstruct the image for SEBS1. Figure 5.10b shows the original data for SEBS1 filtered using the same spatial frequencies as used for FT-UOT. This provides a more direct comparison between the two techniques. Despite this "lowering of playing field", the focused regime image retains greater structural detail than the FT-UOT image (figure 5.7b). Figure 5.10c shows the same data processed with a Gaussian filter, a common approach in medical imaging to suppress noise and improve visual smoothness. While such filtering improves image appearance, it may also hide finer structural details.

5.2 Final discussion

The results discussed above demonstrate that, for the experimental setup used in the experiments, the focused regime produces better images, having higher contrast and better spatial definition. Another factor that should be mentioned is that the acquisition and image reconstruction times for the FT-UOT were about five times more ($\sim$ 500 seconds) than that of the focused regime. The images that were acquired

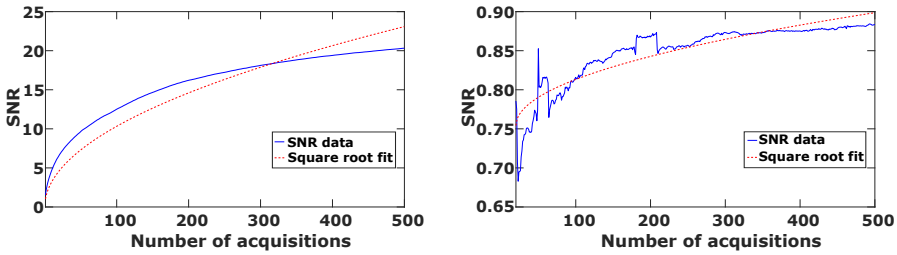

(a) Focused Regime **(b)** FT-UOT

Figure 5.9: SNR as a function of number of acquisitions for both techniques with $\sqrt{x}$ fit indicated with the red-dotted line.

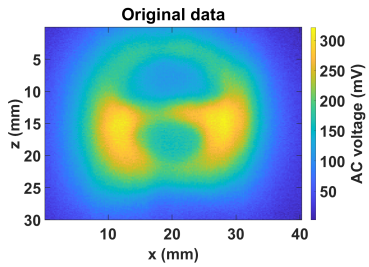

(a) Raw data image of SEBS2.

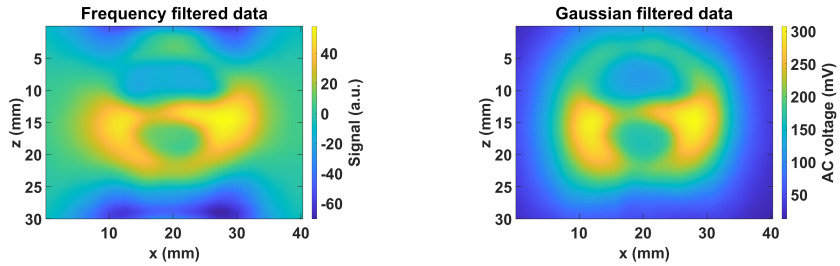

(b) Spatial frequency filtered image of SEBS2. **(c)** Gaussian filtered image of SEBS2.

Figure 5.10: UOT images of SEBS2 after different types of filtering.

through the focused regime showed more details and were faster to acquire as well. One of the main ideas behind FT-UOT is to increase the tagging volume, which leads to more tagged light, and hence to a greater signal. Although this increase in signal was noticed while conducting the experiments, it did not translate into improved image quality. The FT-UOT images also exhibit artifacts in the form of spatially oscillating "wavy" patterns, which degrades image interpretability. Without the focused regime images to act as a baseline, being able to clearly identify and understand inclusion details would be a difficult task. This is mainly due to two reasons. First, the US transducer may not generate the precise spatially structure pressure fields required to accurately encode Fourier components. Second, sound waves diverge as they prop-

agate in tissue. This also causes the acoustic waves to lose their exact structuring, leading to the loss of some information. Another factor that played a role in the increase in acquisition times, except the need to sequentially sample spatial frequencies, was the communications overhead with the US transducer system. However, this can be easily overcome with a better optimized set-up. The resolution of the images acquired through FT-UOT can be improved by using more and maybe even smaller spatial frequencies to image the object, this however will result in increased acquisition times, as well as greater stress on the transducer, as they are not designed to emit complex US patterns.

Chapter 6

Summary

This thesis investigated the feasibility of FT-UOT as an alternative to the conventional focused US regime with the help of AgI and SEBS phantoms. This chapter summarizes the key findings and their implications. Both simulation and experimental approaches were taken to analyze the performance of FT-UOT in comparison to the focused regime. The performance and limitations of FT-UOT are discussed, followed by possible improvements and potential directions of future research.

6.1 Conclusions

A simulation model based on mean photon path lengths, the diffusion equation, and a perturbation approach was implemented to study FT-UOT. The results showed that, in theory, spatially structured US fields can be used to reconstruct UOT images through sampling in the Fourier domain. The simulated reconstructed images demonstrated that FT-UOT is able to recover spatial features comparable to those reconstructed with the original focused US simulation images, thus validating the underlying concept.

Experimental measurements were performed on both AgI and SEBS phantoms. The focused regime consistently produced higher quality images with clearly identifiable inclusions and good contrast. Initial FT-UOT measurements showed limited ability to resolve inclusion features, especially in SEBS phantoms, which were more optically absorbing. By slightly modifying the experimental setup, an increase in signal was achieved. Under the new and improved conditions, FT-UOT was able to reveal inclusion features. The overall location and structure of the inclusions were consistent between the two methods, however the FT-UOT images contained artifacts and had

lower spatial definition. This shows the experimental viability of FT-UOT, but it has its limitations due to practical constraints and improvements would need to be made in order to make FT-UOT competitive with the focused US regime.

Along with image quality, acquisition time of FT-UOT images is another limitation in the setup used in the thesis. With the need to sequentially sample multiple spatial frequencies combined with the system overhead in controlling the transducer, giving rise to substantially longer acquisition times. This can easily be addressed through hardware and software optimization.

Despite these challenges, FT-UOT, in principle, offers several advantages, like the ability to probe a greater volume simultaneously. This has the potential to increase the acousto-optic signal, thus improving the imaging efficiency. It is important to mention that FT-UOT was designed to be implemented with camera-based detection, such as digital holography [52, 53, 64]. In contrast, the implementation used in this work relies on temporally sampled signals. This difference in detection method may limit the direct translation of FT-UOT, though successful results have been shown for PR holography [52].

In conclusion, while FT-UOT does not outperform the focused regime under the studied conditions, it demonstrates strong theoretical foundations. With potential improvements through digital holography and possibly spectral hole burning, FT-UOT cannot be dismissed. Its advantages position it as a worthwhile direction for future development in UOT.

6.2 Future prospects

Several directions can be pursued to help develop UOT and FT-UOT. As discussed earlier, the transducer used in the current setup may not accurately generate the required spatial structuring of the acoustic fields. A natural next step would be to use an improved (or accurate) transducer, combined with camera-based detection schemes like digital holography, that is computationally accelerated with the use of GPUs. Such developments are already underway at the Langevin Institute in Paris. Extending the simulation framework to include more realistic acoustic and optical conditions could also provide deeper insight into limitations of systems and help guide experimental improvements for FT-UOT. Another possible direction is the implementation of FT-UOT using spectral hole burning filters, which have been shown to provide high contrast-to-noise ratio imaging at greater depth [36]. This approach could be explored within the UOT laboratory of the Quantum Information group at Atomic physics at Lund. There has been recent work in surpassing the acoustic resolution

limit using speckle decorrelation in the focused regime also presents an interesting avenue for further [65, 66]. Exploring how such techniques could be integrated with or adapted to FT-UOT may give rise to new possibilities for improving spatial resolution for UOT techniques.

Appendix A

More simulation images

Figure A.1 shows the simulation result for two inclusions. The images are ordered the same way as in figure 4.2, showing the same information, but for two inclusions.

Figure A.2a shows a horizontal cross-section in the *x*-*y* plane at $z = 28.5$ mm in the absence of inclusions, setting a baseline. It is radially symmetric as expected. Figure . Figure A.2b is the focused regime reconstruction in the $x-y$ plane for two inclusions. Figure A.2c is the FT-UOT reconstruction for two inclusions in the $x - y$ plane. Similarly, figures A.2d and A.2e, show the reconstruction in the $x - y$ plane for the focused regime and FT-UOT for one inclusion, respectively. The localized decrease in signal intensity show the location of the inclusion(s).

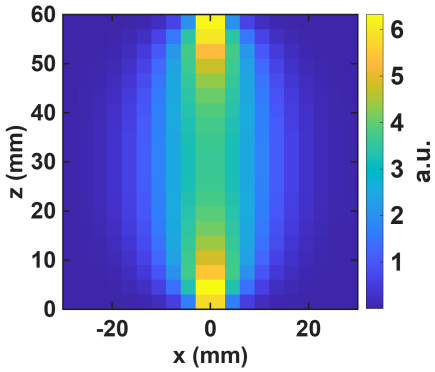

(a) Mean path length in each voxel.

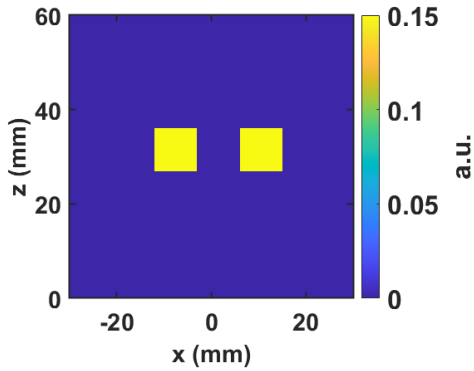

(b) Ground truth image for two inclusions case.

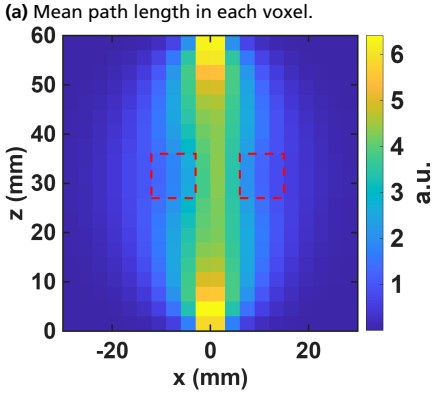

(c) Image constructed through focused regime.

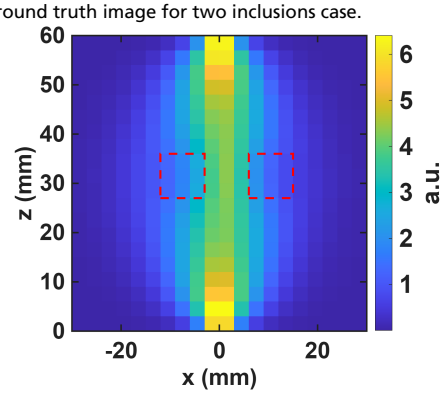

(d) Image reconstructed through FT-UOT.

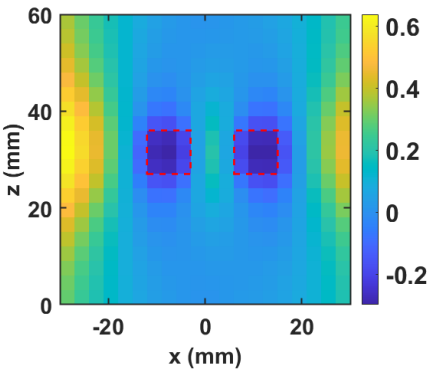

(e) Relative contrast map.

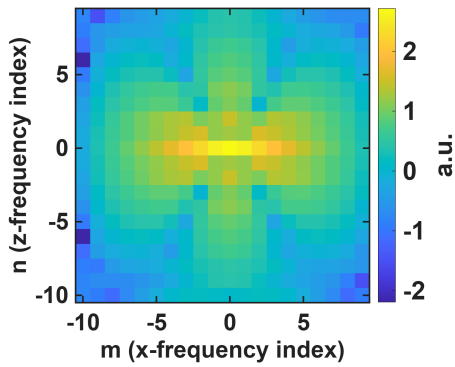

(f) Fourier plane log|S(m,n)|.

Figure A.1: Results for the two inclusion case for the focused regime and FT-UOT. The inclusions are marked with red-dashed lines to indicate their location in the medium.

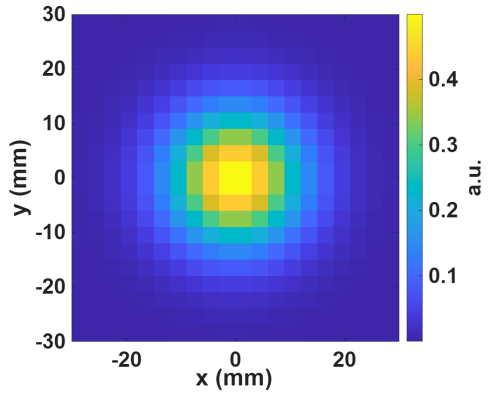

(a) Homogeneous profile in xy plane.

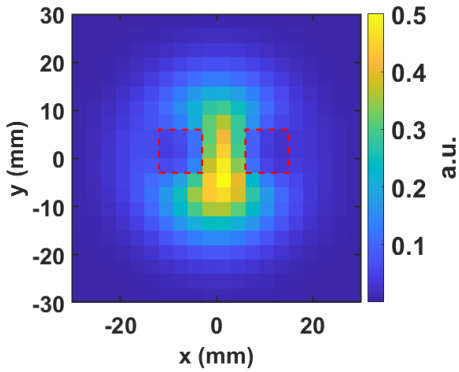

(b) xy plane image at $z = 28.5$ mm for focused regime for two inclusions.

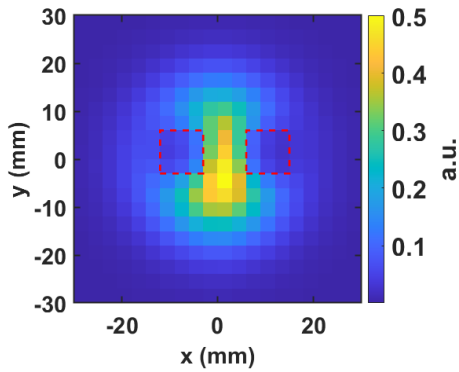

(c) xy plane image at $z = 28.5$ mm for FT-UOT for two inclusions.

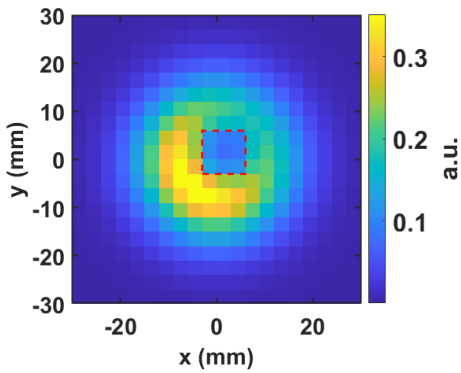

(d) xy plane image at $z = 28.5$ mm for focused regime for one inclusion.

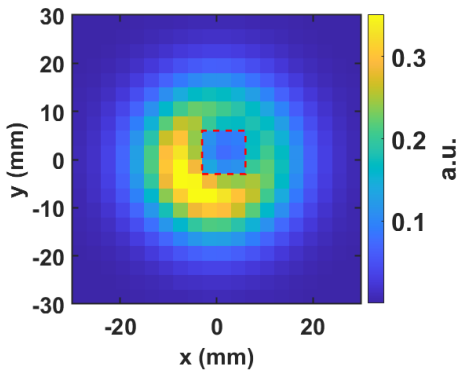

(e) xy plane image at $z = 28.5$ mm for FT-UOT for one inclusion.

Figure A.2: Images in the xy plane at $z = 28.5$ mm. For 1 and 2 inclusion(s).

References

[1] W. C. Röntgen, "On a new kind of rays," *Science*, vol. 3, no. 59, pp. 227–231, 1896.

[2] V. Kajla, A. Gupta, and A. Khatak, "Analysis of X-Ray images with image processing techniques: A review," in *2018 4th International Conference on Computing Communication and Automation (ICCCA)*, 2018, pp. 1–4.

[3] J. H. Scatliff and P. J. Morris, "From Röntgen to Magnetic Resonance Imaging: The History of Medical Imaging," *North Carolina Medical Journal*, vol. 75, no. 2, 2014.

[4] X. Ou, X. Chen, X. Xu, L. Xie, X. Chen, Z. Hong, H. Bai, X. Liu, Q. Chen, L. Li, and H. Yang, "Recent development in X-Ray imaging technology: Future and challenges," *Research*, vol. 2021, 2021.

[5] O. Taubmann, M. Berger, M. Bögel, Y. Xia, M. Balda, and A. Maier, *Computed Tomography*. Cham: Springer International Publishing, 2018, pp. 147–189.

[6] S. Hermena and M. Young, "CT-scan image production procedures," in *StatPearls*. Treasure Island (FL): StatPearls Publishing, 2026.

[7] V. P. Grover, J. M. Tognarelli, M. M. Crossey, I. J. Cox, S. D. Taylor-Robinson, and M. J. McPhail, "Magnetic resonance imaging: Principles and techniques: Lessons for clinicians," *Journal of Clinical and Experimental Hepatology*, vol. 5, no. 3, pp. 246–255, 2015.

[8] K. Martin and K. Ramnarine, *Physics*. Cambridge University Press, 2010, pp. 4–22.

[9] H. Jiang, *Diffuse Optical Tomography: Principles and Applications*. Taylor & Francis, 2010.

[10] T. Durduran, R. Choe, W. B. Baker, and A. G. Yodh, "Diffuse optics for tissue monitoring and tomography," *Reports on Progress in Physics*, vol. 73, no. 7, 2010.

[11] D. Huang, E. A. Swanson, C. P. Lin, J. S. Schuman, W. G. Stinson, W. Chang, M. R. Hee, T. Flotte, K. Gregory, C. A. Puliafito, and J. G. Fujimoto, "Optical coherence tomography," *Science*, vol. 254, no. 5035, pp. 1178–1181, 1991.

[12] A. M. Zysk, F. T. Nguyen, A. L. Oldenburg, D. L. Marks, and S. A. Boppart, "Optical coherence tomography: a review of clinical development from bench to bedside," *Journal of Biomedical Optics*, vol. 12, no. 5, p. 051403, 2007.

[13] L. V. Wang, "Ultrasound-mediated biophotonic imaging: A review of acousto-optical tomography and photo-acoustic tomography," *Disease Markers*, vol. 19, no. 2-3, p. 478079, 2004.

[14] J. Xia, J. Yao, and L. V. Wang, "Photoacoustic tomography: principles and advances," *Electromagnetic waves (Cambridge, Mass.)*, vol. 147, p. 1, 2014.

[15] L. V. Wang and J. Yao, "A practical guide to photoacoustic tomography in the life sciences," *Nature Methods*, vol. 13, no. 8, 2016.

[16] D. S. Elson, R. Li, C. Dunsby, R. Eckersley, and M.-X. Tang, "Ultrasound-mediated optical tomography: a review of current methods," *Interface Focus*, vol. 1, no. 4, pp. 632–648, 2011.

[17] J. Gunther and S. Andersson-Engels, "Review of current methods of acousto-optical tomography for biomedical applications," *Frontiers of Optoelectronics*, vol. 10, no. 3, pp. 211–238, 2017.

[18] A. Zabiliūtė-Karaliūnė, A. Kinos, A. Bengtsson, D. Gustavsson, D. Hill, E. Bukartė, E. K. Svanberg, J. Swartling, K. Shortiss, L. Rippe, M. Dustler, M. Ruchkina, N. Chaudhry, N. Reistad, P. Tatidis, P. R. Bakic, S. Zackrisson, and S. Kröll, "Potential clinical applications of ultrasound optical tomography: Breast tissue characterization and brain imaging," in *European Conferences on Biomedical Optics 2025*. Optica Publishing Group, 2025, p. Tu2A.45.

[19] G. Keiser, *Light-Tissue Interactions*. Singapore: Springer Nature Singapore, 2022, pp. 169–221.

[20] C. Boudoux, *Fundamentals of Biomedical Optics: From Light Interactions with Cells to Complex Imaging Systems*. Pollux, 2017.

[21] A. Bengtsson, "Material and technique development for ultrasound optical tomography using spectral hole burning filters," Doctoral Thesis (compilation), Atomic Physics, 2022.

[22] L. A. Sordillo, Y. Pu, S. Pratavieira, Y. Budansky, and R. R. Alfano, "Deep optical imaging of tissue using the second and third near-infrared spectral windows," *Journal of Biomedical Optics*, vol. 19, no. 5, p. 056004, 2014.

[23] A. M. Smith, M. C. Mancini, and S. Nie, "Second window for in vivo imaging," *Nature Nanotechnology*, vol. 4, no. 11, 2009.

[24] L. V. Wang and H.-i. Wu, *Biomedical Optics*. John Wiley Sons, Ltd.

[25] J. L. Sandell and T. C. Zhu, "A review of in-vivo optical properties of human tissues and its impact on pdt," *Journal of Biophotonics*, vol. 4, no. 11-12, pp. 773–787, 2011.

[26] J. C. Juarez-Ramirez, B. Coyotl-Ocelotl, B. Choi, R. Ramos-Garcia, T. Spezzia-Mazzocco, and J. C. Ramirez-San-Juan, "Improved spatial speckle contrast model for tissue blood flow imaging: effects of spatial correlation among neighboring camera pixels," *Journal of Biomedical Optics*, vol. 28, no. 12, p. 125002, 2023.

[27] D. A. Boas and A. K. Dunn, "Laser speckle contrast imaging in biomedical optics," *Journal of Biomedical Optics*, vol. 15, no. 1, p. 011109, 2010.

[28] D. C. Park and D. W. Park, "Ultrasound speckle decorrelation-based blood flow measurements," *Ultrasound in Medicine & Biology*, vol. 49, no. 7, pp. 1491–1498, 2023.

[29] R. Jones and C. Wykes, *Holographic and Speckle Interferometry*. Cambridge: Cambridge University Press, 1988, vol. 6.

[30] J. Williams. (2021) Yale team produces memory from speckle patterns.

[31] M. Gross, P. Goy, B. C. Forget, M. Atlan, F. Ramaz, A. C. Boccara, and A. K. Dunn, "Heterodyne detection of multiply scattered monochromatic light with a multipixel detector," *Opt. Lett.*, vol. 30, pp. 1357–1359, 2005.

[32] Y. Liu, P. Lai, C. Ma, X. Xu, A. A. Grabar, and L. V. Wang, "Optical focusing deep inside dynamic scattering media with near-infrared time-reversed ultrasonically encoded (TRUE) light," *Nature Communications*, vol. 6, no. 1, 2015.

[33] L. Brillouin, "Diffusion de la lumière et des rayons X par un corps transparent homogène - Influence de l'agitation thermique," *Ann. Phys.*, vol. 9, no. 17, pp. 88–122, 1922.

[34] P. Debye and F. W. Sears, "On the scattering of light by supersonic waves," *Proceedings of the National Academy of Sciences*, vol. 18, no. 6, pp. 409–414, 1932.

[35] R. Lucas and P. Biquard, "Propriétés optiques des milieux solides et liquides soumis aux vibrations élastiques ultra sonores," *J. Phys. Radium*, vol. 3, no. 10, pp. 464–477, 1932.

[36] A. Bengtsson, D. Hill, K. Shortiss, L. Rippe, and S. Kröll, "Comparison of contrast-to-noise ratios of different detection methods in ultrasound optical tomography," *Biomed. Opt. Express*, vol. 13, pp. 4834–4850, 2022.

[37] C. Dupuy, "Image reconstruction for acousto-optics: Towards quantitative imaging," 2017.

[38] J.-P. Monchalin, R. Héon, P. Bouchard, and C. Padioleau, "Broadband optical detection of ultrasound by optical sideband stripping with a confocal Fabry–Pérot," *Applied Physics Letters*, vol. 55, no. 16, 1989.

[39] Y. Li, H. Zhang, C. Kim, K. H. Wagner, P. Hemmer, and L. V. Wang, "Pulsed ultrasound-modulated optical tomography using spectral-hole burning as a narrowband spectral filter," *Applied Physics Letters*, vol. 93, no. 1, 2008.

[40] A. Bengtsson, D. Hill, M. Li, M. Di, M. Cinthio, T. Erlöv, S. Andersson-Engels, N. Reistad, A. Walther, L. Rippe, and S. Kröll, "Characterization and modeling of acousto-optic signal strengths in highly scattering media," *Biomed. Opt. Express*, vol. 10, pp. 5565–5584, 2019.

[41] A. Kinos, Q. Li, L. Rippe, and S. Kröll, "Development and characterization of high suppression and high étendue narrowband spectral filters," *Appl. Opt.*, vol. 55, pp. 10 442–10 448, 2016.

[42] D. Hill, "Development of models, methods, and materiel for deep tissue imaging using light, ultrasound, and spectral-hole burning," Doctoral Thesis (compilation), Atomic Physics, 2022.

[43] L. V. Wang, "Mechanisms of ultrasonic modulation of multiply scattered coherent light: an analytic model," *Physical Review Letters*, vol. 87, no. 4, p. 043903, 2001.

[44] ——, "Mechanisms of ultrasonic modulation of multiply scattered coherent light: a monte carlo model," *Optics letters*, vol. 26, no. 15, pp. 1191–1193, 2001.

[45] A. Kinos, "Frequency shifting of light via multiple ultrasound waves in scattering media," *Biomedical Optics Express*, vol. 15, no. 12, pp. 7066–7076, 2024.

[46] D. Hill, A. Bengtsson, T. Erlöv, M. Cinthio, and S. Kröll, "Acousto-optic interaction strengths in optically scattering media using high pressure acoustic pulses," *Biomed. Opt. Express*, vol. 12, pp. 3196–3213, 2021.

[47] J.-B. Laudereau, E. B. à La Guillaume, V. Servois, P. Mariani, A. A. Grabar, M. Tanter, J.-L. Gennisson, and F. Ramaz, "Multi-modal acousto-optic/ultrasound imaging of ex vivo liver tumors at 790 nm using a Sn2P2S6

wavefront adaptive holographic setup," *Journal of Biophotonics*, vol. 8, no. 5, pp. 429–436, 2015.

[48] M. Kim, S. Im, I. Park, D. Kim, E. S. Kim, J. Joseph, and J. Yoon, "Fabrication of agar-based tissue-mimicking phantom for the technical evaluation of biomedical optical imaging systems," *Current Applied Physics*, vol. 61, pp. 80–85, 2024.

[49] A. Khodaverdi, M. Cinthio, E. Reistad, T. Erlöv, M. Malmsjö, S. Zackrisson, and N. Reistad, "Optical tuning of copolymer-in-oil tissue-mimicking materials for multispectral photoacoustic imaging," *Biomedical Physics & Engineering Express*, vol. 10, 2024.

[50] M. Bocoum, J.-L. Gennisson, J.-B. Laudereau, A. Louchet-Chauvet, J.-M. Tualle, and F. Ramaz, "Structured ultrasound-modulated optical tomography," *Applied optics*, vol. 58, no. 8, pp. 1933–1940, 2019.

[51] M. Bocoum, F. Figliolia, J.-P. Huignard, F. Ramaz, and J.-M. Tualle, "Suppression of the Talbot effect in Fourier transform acousto-optic imaging," *Appl. Opt.*, vol. 62, no. 18, 2023.

[52] M. Bocoum, J.-L. Gennisson, A. A. Grabar, F. Ramaz, and J.-M. Tualle, "Reconstruction of bi-dimensional images in fourier-transform acousto-optic imaging," *Optics Letters*, vol. 45, no. 17, pp. 4855–4858, 2020.

[53] L. Dutheil, M. Bocoum, M. Fink, S. M. Popoff, F. Ramaz, and J.-M. Tualle, "Fourier transform acousto-optic imaging with off-axis holographic detection," *Applied optics*, vol. 60, no. 24, pp. 7107–7112, 2021.

[54] L. Wang, S. L. Jacques, and L. Zheng, "Mcml—monte carlo modeling of light transport in multi-layered tissues," *Computer methods and programs in biomedicine*, vol. 47, no. 2, pp. 131–146, 1995.

[55] T. S. Leung and S. Powell, "Fast monte carlo simulations of ultrasound-modulated light using a graphics processing unit," *Journal of biomedical optics*, vol. 15, no. 5, pp. 055 007–055 007, 2010.

[56] Y. Huang, M. Cua, J. Brake, Y. Liu, and C. Yang, "Investigating ultrasound–light interaction in scattering media," *Journal of Biomedical Optics*, vol. 25, no. 2, p. 025002, 2020.

[57] J. L. Hollmann, R. Horstmeyer, C. Yang, and C. A. DiMarzio, "Diffusion model for ultrasound-modulated light," *Journal of biomedical optics*, vol. 19, no. 3, pp. 035 005–035 005, 2014.

[58] X. Wang, "The diffusion equation in multilayered rectangular biological tissue with finite thickness," *Optik*, vol. 180, pp. 144–150, 2019.

[59] S. Šušnjar, A. Kinos, P. R. Bakic, S. Zackrisson, F. Martelli, J. Swartling, S. Kröll, and N. Reistad, "Analytical model for rapid simulation of ultrasound optical tomography images based on mean photon path lengths," *Optics Express*, vol. 33, no. 19, pp. 40 091–40 120, 2025.

[60] D. Hill, A. Bengtsson, T. Erlöv, M. Cinthio, and S. Kröll, "First principle simulation package for arbitrary acousto-optic interaction in scattering materials," in *European Conferences on Biomedical Optics 2021 (ECBO)*. Optica Publishing Group, 2021, p. ES1C.6.

[61] S. Sakadžić and L. V. Wang, "Ultrasonic modulation of multiply scattered coherent light: an analytical model for anisotropically scattering media," *Physical Review E*, vol. 66, no. 2, p. 026603, 2002.

[62] ——, "Modulation of multiply scattered coherent light by ultrasonic pulses: an analytical model," *Physical Review E—Statistical, Nonlinear, and Soft Matter Physics*, vol. 72, no. 3, p. 036620, 2005.

[63] F. Martelli, T. Binzoni, S. Del Bianco, A. Liemert, and A. Kienle, "Light propagation through biological tissue and other diffusive media: theory, solutions, and validations." SPIE Bellingham, WA, USA, 2022.

[64] K. Barjean, F. Ramaz, and J.-M. Tualle, "Theoretical study of fourier-transform acousto-optic imaging," *Journal of the Optical Society of America A*, vol. 33, no. 5, pp. 854–862, 2016.

[65] M. Rosenfeld, G. Weinberg, D. Doktofsky, Y. Li, L. Tian, and O. Katz, "Acousto-optic ptychography," *Optica*, vol. 8, no. 6, 2021.

[66] D. Doktofsky, M. Rosenfeld, and O. Katz, "Acousto optic imaging beyond the acoustic diffraction limit using speckle decorrelation," *Communications Physics*, vol. 3, no. 1, 2020.